A numerical two-scale homogenization scheme: the FE^2-method

Jörg Schröder

Institute of mechanics, Dept. Civil Engineering, Fac. of Engineering,
University of Duisburg-Essen
Corresponding author: j.schroeder@uni-due.de

Abstract A wide class of micro-heterogeneous materials is designed to satisfy the advanced challenges of modern materials occurring in a variety of technical applications. The effective macroscopic properties of such materials are governed by the complex interaction of the individual constituents of the associated microstructure. A *sufficient* macroscopic phenomenological description of these materials up to a certain order of accuracy can be very complicated or even impossible. On the contrary, a whole resolution of the fine scale for the macroscopic boundary value problem by means of a classical discretization technique seems to be too elaborate.

Instead of developing a macroscopic phenomenological constitutive law, it is possible to attach a representative volume element ($\mathcal{RVE}$) of the microstructure at each point of the macrostructure; this results in a two-scale modeling scheme. A discrete version of this scheme performing finite element (FE) discretizations of the boundary value problems on both scales, the macro- and the micro-scale, is denoted as the FE^2-method or as the multilevel finite element method. The main advantage of this procedure is based on the fact that we do not have to define a macroscopic phenomenological constitutive law; this is replaced by suitable averages of stress measures and deformation tensors over the microstructure.

Details concerning the definition of the macroscopic quantities in terms of their microscopic counterparts, the definition/construction of boundary conditions on the $\mathcal{RVE}$ as well as the consistent linearization of the macroscopic constitutive equations are discussed in this contribution.

Furthermore, remarks concerning stability problems on both scales as well as their interactions are given and representative numerical examples for elasto-plastic microstructures are discussed.

J. Schröder, K. Hackl (Eds.), *Plasticity and Beyond*, CISM International Centre for Mechanical Sciences, DOI 10.1007/978-3-7091-1625-8_1, © CISM, Udine 2014

1 Introduction

For the analysis of micro-heterogeneous materials, we define two different scales, the macroscopic scale (coarse scale) and the microscopic scale (fine scale). The fine scale is assumed to be the scale of the heterogeneities of characteristic length l, whereas the characteristic length of the coarse scale is denoted by L. If we assume that the domain size at the fine scale is sufficient for homogenization requirements, then the *separation of scales* expressed by

$$l \ll L \tag{1}$$

has to hold. A homogenized – that means effective macroscopic – description of the micro-heterogeneous material requires the definition of a representative volume element ($\mathcal{RVE}$) or a *statistically homogeneous volume element*, which is here assumed to be possible. In classical works, effective quantities of micro-heterogeneous media, such as stiffness or compliance tensors, have been discussed by Voigt (1910) and Reuss (1929). The arithmetical mean value of Voigt and the harmonic mean value of Reuss were shown later to be upper and lower bounds of effective parameters, see Hill (1965b, 1964a,b, 1963). However, the gap between these approximations can be quite wide, see e.g. Babuska (1976). General procedures for the derivation of inequalities between various moduli of mixtures have been discussed by Hill (1963) and Kröner (1971). A variety of methods for the computation of overall properties of micro-heterogeneous materials are documented in the monograph Nemat-Nasser and Hori (1999).
A fundamental assumption for the scale-transition is the *macro-homogeneity condition*, also denoted as *Hill condition* or *Hill-Mandel condition*, which asserts the equality of the virtual work between both scales, see Hill (1965a, 1963), Mandel and Dantu (1963), Mandel (1972). There are several "additive" mechanical quantities which could be averaged over the representative volume element when transferred to the macro-scale, e.g. the mass, internal energy, entropy and dissipation. Furthermore, macroscopic measures of plastic work for micro-heterogeneous materials have been analyzed in Hill (1971).

A suitable framework for the solution of two-scale problems is the mathematical homogenization theory. There, it is usually assumed that the microstructure is locally built by the spatial repetition of a suitable, very small part of the whole microstructure, a unit cell. Thus, it is assumed that the morphology and the distribution of the material properties are periodic functions of the microscopic spatial parametrization y. As an introductionary example we consider a simple one-dimensional bar. For this purpose, let

the periodic function $EA(y)$ denote the axial stiffness of a bar, $u(\overline{x}, y)$ the axial displacement, $\overline{x}$ the parametrization of the coarse scale, and $n(\overline{x})$ the distributed axial load, then the axial displacements of the bar are described by the differential equation

$$\frac{d}{d\overline{x}} N(\overline{x}, y) + n(\overline{x}) = 0 \quad \text{with} \quad N(\overline{x}, y) := EA(y) \, \frac{du(\overline{x}, y)}{d\overline{x}} \, . \tag{2}$$

The mathematical homogenization theory is based on the double scale asymptotic expansion of the yet unknown y-periodic field variable $u(\overline{x}, y)$, i.e.,

$$u(\overline{x}, y) = u^{(0)}(\overline{x}, y) + \epsilon \, u^{(1)}(\overline{x}, y) + \epsilon^2 \, u^{(2)}(\overline{x}, y) + \cdots \, , \tag{3}$$

where ϵ, defined as the microscopic to macroscopic dimension ratio (l/L), is a very small number. The asymptotic expansion (3) has to be substituted into the underlying partial differential equation with oscillating coefficients. Applying the chain rule, i.e.,

$$\frac{d}{d\overline{x}} N(\overline{x}, y) = \frac{\partial N(\overline{x}, y)}{\partial \overline{x}} + \epsilon^{-1} \frac{\partial N(\overline{x}, y)}{\partial y} \, , \tag{4}$$

yields a set of equations with factors in powers of ϵ. Equating the terms of the different orders of ϵ with zero yields the set of differential equations, which have to be solved. Fundamentals of this framework can be found in Bensoussan et al. (1978), Sanchez-Palencia and Zaoui (1986) and Bakhvalov and Panasenko (1984). Based on this approach, a computational homogenization framework in the field of linear elasticity as well as the application of adaptive finite element methods has been proposed in Guedes and Kikuchi (1990). Extensions of this method to locally non-periodic microheterogeneous media are given by Fish and Wagiman (1993). A framework of a two-scale homogenization technique using a Voronoi cell finite element formulation has been proposed by Ghosh et al. (1995). Generalized convergence arguments for the interpretation of the homogenized variational equations have been used by Terada and Kikuchi (2001). An extension of the latter simultaneous two-scale method to geometrical nonlinear formulations of the associated two-scale boundary value problems in a material and a spatial setting has been developed in Terada et al. (2003). Several mathematical aspects of homogenization theory are discussed in Tartar (2000). For the treatment of finite thermoelasticity in this scheme, we refer to Temizer (2012).

A homogenization technique without recourse to the two-scale asymptotic expansion is governed by the above mentioned *Hill-Mandel condition*.

Here, the boundary value problems on the macro- and on the micro-scale are prescribed by the balance of linear and angular momentum and suitable boundary conditions on both scales, where the micro-scale is approximated by means of a representative volume element. A summary of recent developments in this field of applied computational mechanics of the overall description of micro-heterogeneous materials up to the mid 1980's is given in Suquet (1987). In this context we also refer to Michel et al. (1999) where the boundary value problem on the micro-scale is solved using the Finite-Element-Method (FEM) and, alternatively, using a Fast Fourier Transformation. The authors also discuss the constraints on discrete unknown displacements arising when periodic boundary conditions are used.
A multilevel finite element method (FE^2-method) for nonlinear heterogeneous systems has been discussed by Smit et al. (1998), where the authors implemented their algorithms in an Updated Lagrange environment. Another FE^2-method for the analysis of the elasto-viscoplastic behavior of fiber-reinforced composite materials was presented by Feyel and Chaboche (2000), where the tangent matrix has been approximated by a perturbation method. A framework for geometrically and/or physically linear/nonlinear homogenization techniques in the sense of the FE^2-method has been developed by Miehe et al. (1999a,b), including a closed-form representation of the macroscopic (homogenized) tangent moduli. In order to design "deformation-driven" microstructures, Miehe and Koch (2002) proposed a Lagrangian multiplier method for the computational treatment of the constraints arising from the different boundary conditions: i) linear displacements, ii) constant tractions, and iii) periodic displacements in combination with antiperiodic tractions; for the discussion of the distinct boundary conditions, see also van der Sluis et al. (2000), Terada et al. (2000), Kouznetsova et al. (2001), Miehe and Bayreuther (2007) and Perić et al. (2011). A family of algorithms and matrix representations of overall stresses and tangent moduli of discretized micro-heterogeneous materials at finite strains is descriped in Miehe (2003). Different methods for the computation of the macroscopic tangent, e.g. the penalty method, have been investigated in Temizer and Wriggers (2008).

The nature of finite deformation continuum mechanics is the non-uniqueness of solutions at specific thermodynamic states. As an example, this can be associated to stability problems like buckling of columns under compressive loadings. Although in micro-heterogeneous materials, like aligned fiber-reinforced composites, cellular solids or in general arbitrary arrangements of inhomogeneities, buckling phenomena may occur on the micro-scale. A challenging issue in homogenization schemes at finite strains is the ana-

lysis of instabilities at the macro- and micro-scale and their interactions. In general, we distinguish between structural instabilities and material instabilities: structural instabilities are associated to the non-uniqueness of the underlying boundary value problem, whereas material instabilities are understood as the violation of the Legendre-Hadamard-condition (loss of rank-one convexity) of the free-energy. Nevertheless, there exits a relation between material instabilities on the macro-scale and specific structural instabilities on the micro-scale. Abeyaratne and Triantafyllidis (1984) studied the macroscopic material instability occuring in nonlinear elastic composites with periodically arranged voids. It was shown that a homogenized material instability occurs although the matrix material was polyconvex in the sense of Ball (1977b). Bifurcation modes of fiber-reinforced composites as well as possible macroscopic material instabilities have been analyzed in Triantafyllidis and Maker (1985). Structural instability problems on the micro-scale are associated to the homogenization of a nonconvex boundary value problem on the micro-scale, see Müller (1987). The main challenge here is the a priori unknown size of the $\mathcal{RVE}$. A systematic investigation of the problems pointed out in Abeyaratne and Triantafyllidis (1984) and Triantafyllidis and Maker (1985) is given in Geymonat et al. (1993). Applying a Bloch-wave ansatz to a fiber-reinforced composite, the authors showed that the onset of a bifurcation on the micro-scale corresponding to the long-wavelength limit (infinite wavelength) leads to a macroscopic material instability. A detailed computational homogenization analysis of structural instabilities on the micro-scale and possible material instabilities on the macro-scale as well as their interactions is performed in Miehe et al. (2002), in this context see also Agoras et al. (2009) and Aubert et al. (2008). A microscopic bifurcation condition of cellular solids, like elastic cellular honeycombs, have been presented in Ohno et al. (2002). A procedure, based on a block-diagonalization method for periodic microstructures, for the estimation of the number of unit cells necessary for the definition of a $\mathcal{RVE}$ of cellular solids in microscopic bifurcation problems has been proposed in Saiki et al. (2002). In the context of homogenization of non-convex integral functionals and especially for the relation between linearization and homogenization in finite elasticity, we refer to Müller and Neukamm (2011). For the treatment of localized failure with softening in this multi-scale approach see Hautefeuille et al. (2012).

If the classical assumption of scale separation does not hold or if it is necessary to capture size dependency, then in general higher-order homogenization techniques can be applied. A second-order homogenization scheme, implying a second gradient continuum on the macro-scale and a remaining classical continuum on the micro-scale, has been proposed by Geers et al.

(2001, 2003) and Kouznetsova et al. (2004). A multilevel finite element method coupling a classical continuum, a Cauchy continuum, on the fine scale with a Cosserat continuum at the coarse scale has been proposed by Feyel (2003). A critical analysis of the two-scale homogenization of macroscopic second gradient and micromorphic models based on a Cauchy continuum on the fine scale with emphasis on non-homogeneous boundary conditions is given by Forest and Trinh (2011), in this context see also Forest (2002) and Jänicke et al. (2009). An application of the computational homogenization scheme for structured thin sheets has been proposed by Geers et al. (2007) and Gruttmann and Wagner (2013). Here, the $\mathcal{RVE}$ resolves the full thickness of the thin sheet and the nature of the coupling of deformation between the shell-type macro-scale and the microstructure is of second-order.
Another non-classical approach, denoted as a multi-scale strategy for *strongly coupled scales*, has been proposed by Ibrahimbegović and Markovič (2003). Here, the authors attach a part of the microstructure at each finite element of the macro-scale, for details see Markovic et al. (2005) and Niekamp et al. (2009). This is in contrast to the *weakly coupled scales*, where we attach an $\mathcal{RVE}$ of the microstructure at each point of the macrostructure, i.e., at each Gauss point in the discrete version obtained from the FE^2-method.

Recent developments are concerned with direct two-scale homogenization techniques for thermo-mechanically coupled problems, Özdemir et al. (2008), and for electro-mechanically coupled problems concerning the general localization and homogenization scheme, Schröder (2009), as well as the numerical treatment Schröder and Keip (2011, 2012).
Another important topic is the characterization of random microstructures, Ohser and Mücklich (2000), and the identification of statistically representative volume elements, see e.g. Kanit et al. (2003), Stroeven and Askes (2004), Temizer and Zohdi (2007). From the computational point of view, the application of statistically similar representative volume elements, which have less complexity than the original random microstructure, could lead to a significant reduction in computation time. Basic considerations for the definition and optimization procedures based on suitable statistical measure are discussed in Povirk (1995), Ostoja-Starzewski (2006), Balzani et al. (2009, 2010), Schröder et al. (2010), Ambrozinski et al. (2012), in this context see also Swaminathan et al. (2006) and Zohdi and Wriggers (2005). Details on the construction of statistically similar representative volume elements are presented in the contribution by Balzani et al. in this book.

2 Direct Micro-Macro Transition Approach

For the analysis of micro-heterogeneous materials, where we want to take into account the microstructure directly, the transition between the macro- and the micro scale has to be defined, cf. Fig. 1. The direct micro-macro homogenization scheme, based on the finite element discretization of both scales, allows for the computation of macroscopic boundary value problems in consideration of $\mathcal{RVE}s$, which should represent the main characteristics of the associated micro-continuum.

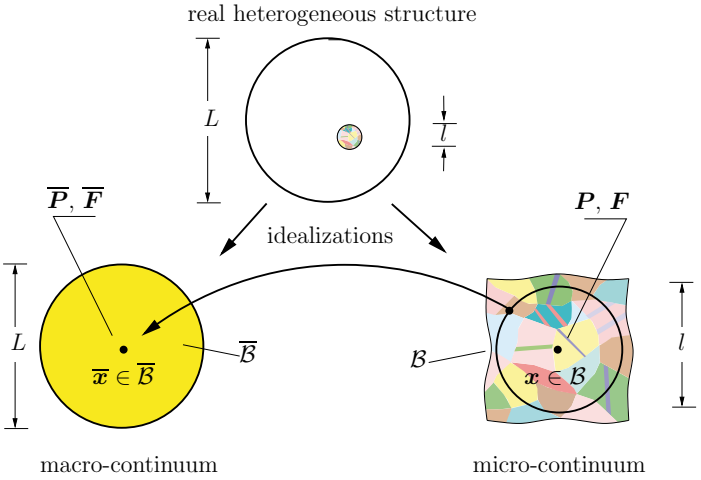

Figure 1. Schematic illustration of the direct homogenization procedure. Notation: macroscopic first Piola-Kirchhoff stresses $\overline{\boldsymbol{P}}$ and deformation gradient $\overline{\boldsymbol{F}}$; their microscopic counterparts are denoted by $\boldsymbol{P}$ and $\boldsymbol{F}$, taken from Schröder et al. (2010)

Since the definition of the individual scales, like macro-, meso- and micro-scale, is somewhat arbitrary, we denote the coarse and fine scale as the macro- and micro-scale, respectively. The main technical ingredients for the two-scale homogenization procedure for mechanical problems are:

- Definition of a $\mathcal{RVE}$ and choosing suitable boundary conditions: The boundary conditions for the microscopic boundary value problem are in general not given a priori. Suitable boundary conditions can be derived by the Hill-Mandel condition, which equates the virtual macroscopic work with the averaged virtual work performed within the $\mathcal{RVE}$.
- Discretization of the microscopic boundary value problem.
- Discretization of the macroscopic boundary value problem.

The main advantage of a direct two-scale homogenization scheme is that we do not have to define a macroscopic phenomenological constitutive law; this is replaced by suitable averages over the $\mathcal{RVE}$. Nevertheless, we have to set up constitutive models for the individual phases on the fine scale. If the local distributions of the deformation and stress measures within the $\mathcal{RVE}$ are computed, we can calculate their macroscopic counterparts by suitable surface or volume integrals over the representative volume element, which are attached at each macroscopic point. Therefore, the numerical micro-to-macro procedure is based on the following consecutive steps:

a) *Localization step, boundary value problem on the micro-scale*: computation of the local distribution of the deformation and stress measures within the $\mathcal{RVE}$ by solving the weak form of the balance of linear momentum.

b) *Homogenization step*: computation of the macroscopic quantities, e.g. the first Piola-Kirchhoff stresses, by means of suitable averages.

c) *Boundary value problem on the macro-scale*: solving the weak form of balance of linear momentum on the coarse scale.

These steps have to be repeated until convergence on both scales is obtained.

2.1 Boundary value problem on the macro-scale

Let the reference configuration of the body of interest on the macroscopic scale $\overline{\mathcal{B}}_0 \subset R^3$ be parameterized in $\overline{\boldsymbol{X}}$. The macroscopic nonlinear deformation map is denoted as $\overline{\boldsymbol{\varphi}}_t(\overline{\boldsymbol{X}})$; it maps points $\overline{\boldsymbol{X}}$ of the reference configuration onto points $\overline{\boldsymbol{x}}$ of the actual configuration $\overline{B}_t$, see Figure 2. The fundamental deformation measure is the macroscopic deformation gradient, defined by

$$\overline{\boldsymbol{F}}(\overline{\boldsymbol{X}}) := \mathrm{Grad}_{\overline{X}}[\overline{\boldsymbol{\varphi}}_t(\overline{\boldsymbol{X}})] \quad \text{with} \quad \overline{F}^a{}_A := \frac{\partial \overline{x}^a}{\partial \overline{X}^A}\,, \tag{5}$$

which maps macroscopic infinitesimal line elements $d\overline{\boldsymbol{X}}$ from the reference configuration to the current configuration, i.e.,

$$d\overline{\boldsymbol{x}} = \overline{\boldsymbol{F}}\, d\overline{\boldsymbol{X}}\,. \tag{6}$$

Let $d\overline{\boldsymbol{A}} = \overline{\boldsymbol{N}}\, d\overline{A}$ and $d\overline{\boldsymbol{a}} = \overline{\boldsymbol{n}}\, d\overline{a}$ denote the infinitesimal vectorial area elements with respect to the reference and current configuration, repectively. The transformation between the quantities is

$$d\overline{\boldsymbol{a}} = [\mathrm{Cof}\, \overline{\boldsymbol{F}}]\, d\overline{\boldsymbol{A}} \quad \text{with} \quad \mathrm{Cof}\, \overline{\boldsymbol{F}} = \overline{J}\, \overline{\boldsymbol{F}}^{-T}\,, \tag{7}$$

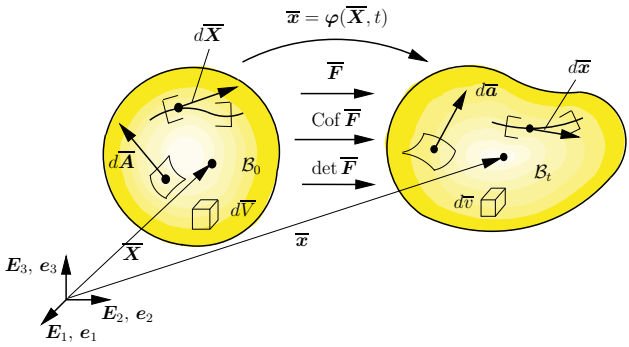

Figure 2. Mapping of infinitesimal line-, vectorial area- and volume-elements from the reference to the actual configuration at the macro-scale.

using Nanson's formula and the abbreviation $\overline{J} = \det \overline{\boldsymbol{F}}$ for their Jacobian determinant. The relation between the macroscopic infinitesimal volume elements $d\overline{V}$ of the reference and $d\overline{v}$ of the current configuration reads

$$d\overline{v} = \overline{J}\, d\overline{V}\,. \tag{8}$$

As a suitable deformation measure, we introduce the macroscopic right Cauchy-Green tensor

$$\overline{\boldsymbol{C}} := \overline{\boldsymbol{F}}^T \overline{\boldsymbol{F}}\,. \tag{9}$$

With the first Piola-Kirchhoff stress tensor $\overline{\boldsymbol{P}}$ the Kirchhoff stresses, the Cauchy stresses and the second Piola-Kirchhoff stresses can be computed by

$$\overline{\boldsymbol{\tau}} = \overline{\boldsymbol{P}}\,\overline{\boldsymbol{F}}^T\,, \quad \overline{\boldsymbol{\sigma}} = \frac{1}{\overline{J}}\,\overline{\boldsymbol{P}}\,\overline{\boldsymbol{F}}^T \quad \text{and} \quad \overline{\boldsymbol{S}} = \overline{\boldsymbol{F}}^{-1}\,\overline{\boldsymbol{P}}\,, \tag{10}$$

respectively. The balance of linear momentum at the macroscopic scale, neglecting acceleration terms, requires

$$\mathrm{Div}_{\overline{X}}\overline{\boldsymbol{P}} + \overline{\boldsymbol{f}} = \boldsymbol{0}\,. \tag{11}$$

Furthermore, the macroscopic balance of moment of momentum, i.e.,

$$\overline{\boldsymbol{P}}\,\overline{\boldsymbol{F}}^T = \overline{\boldsymbol{F}}\,\overline{\boldsymbol{P}}^T \tag{12}$$

is assumed to be satisfied a priori by symmetry requirements of the macroscopic Kirchhoff stress tensor.

2.2 Boundary value problem on the micro-scale

In analogy to the description of the mechanical quantities on the macro-scale, we parametrize the reference placement of the $\mathcal{RVE}$ on the micro-scale $\mathcal{B}_0 \subset \mathbb{R}^3$ with $\boldsymbol{X}$. The nonlinear deformation map on the micro-scale is denoted as $\boldsymbol{\varphi}_t(\boldsymbol{X})$, which maps points $\boldsymbol{X}$ of the reference placement onto points $\boldsymbol{x}$ of the current placement B_t.

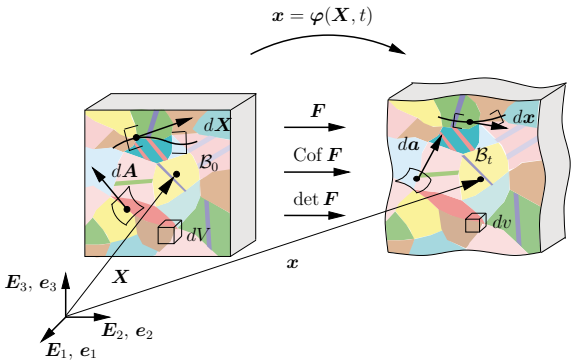

Figure 3. Transport theorems at the micro-scale: Mapping of infinitesimal geometrical elements from the reference to the actual configuration.

The microscopic deformation gradient is defined by

$$\boldsymbol{F}(\boldsymbol{X}) := \mathrm{Grad}_X[\boldsymbol{\varphi}_t(\boldsymbol{X})] \quad \text{with} \quad F^a{}_A := \frac{\partial x^a}{\partial X^A}\,, \tag{13}$$

which maps microscopic infinitesimal line elements $d\boldsymbol{X}$ from the reference configuration to the current configuration, i.e.,

$$d\boldsymbol{x} = \boldsymbol{F}\, d\boldsymbol{X}\,. \tag{14}$$

The transformation of the infinitesimal vectorial area elements of the reference configuration $d\boldsymbol{A} = \boldsymbol{N}\, dA$ to the area elements of the current configuration $d\boldsymbol{a} = \boldsymbol{n}\, da$ is given by

$$d\boldsymbol{a} = [\mathrm{Cof}\, \boldsymbol{F}]d\boldsymbol{A} \quad \text{with} \quad \mathrm{Cof}\, \boldsymbol{F} = J\, \boldsymbol{F}^{-T}\,, \tag{15}$$

using the abbreviation $J = \det \boldsymbol{F}$. The microscopic infinitesimal volume elements dV and dv of the reference and current configuration, respectively, transform with

$$dv = J\, dV\,. \tag{16}$$

As further deformation measures, we introduce the microscopic right Cauchy-Green tensor and the microscopic Finger tensor

$$\boldsymbol{C} := \boldsymbol{F}^T \boldsymbol{F} \quad \text{and} \quad \boldsymbol{b} := \boldsymbol{F} \boldsymbol{F}^T , \tag{17}$$

respectively. Starting from the microscopic first Piola-Kirchhoff stress tensor $\boldsymbol{P}$, we can compute the microscopic Kirchhoff-, Cauchy- and second Piola-Kirchhoff stresses by

$$\boldsymbol{\tau} = \boldsymbol{P} \boldsymbol{F}^T , \quad \boldsymbol{\sigma} = \frac{1}{J} \boldsymbol{\tau} \quad \text{and} \quad \boldsymbol{S} = \boldsymbol{F}^{-1} \boldsymbol{P} , \tag{18}$$

respectively. The balance of linear momentum, neglecting body forces, is given by

$$\mathrm{Div}_X \boldsymbol{P} = \boldsymbol{0} \quad \text{or} \quad \mathrm{div}_x \boldsymbol{\sigma} = \boldsymbol{0} , \tag{19}$$

with respect to the reference and actual placement, respectively. Equation $(19)_2$ is derived from $(19)_1$ by setting $\boldsymbol{P} = \boldsymbol{\sigma} \mathrm{Cof} \boldsymbol{F}$ and applying the Piola identity

$$\mathrm{Div}_X [\mathrm{Cof} \boldsymbol{F}] = \boldsymbol{0} . \tag{20}$$

The balance of moment of momentum

$$\boldsymbol{P} \boldsymbol{F}^T = \boldsymbol{F} \boldsymbol{P}^T . \tag{21}$$

is assumed to be satisfied a priori by symmetry requirements of the Kirchhoff stress tensor, which are guaranteed by the constitutive modeling.

2.3 Macro-variables and microscopic counterparts

An extension of the micro-macro transition framework from small to finite strains has been given in Hill (1972). The determinant $\overline{J}$ of the macroscopic deformation gradient is related to its microscopic counterpart by the volume averages

$$\overline{J} = \frac{1}{V} \int_{\mathcal{B}_0} J \, dV = \frac{1}{V} \int_{\mathcal{B}_t} dv = \frac{v}{V} , \tag{22}$$

here V denotes the reference and v the actual volume of the $\mathcal{RVE}$. Let us assume that the $\mathcal{RVE}$ in its reference placement has a hole $\mathcal{L}_0$ with boundary $\partial \mathcal{L}_0$, then the volume average of deformation gradient can be expressed by

$$\frac{1}{V} \int_{\mathcal{B}_0} \boldsymbol{F} \, dV = \frac{1}{V} \int_{\partial \mathcal{B}_0} \boldsymbol{x} \otimes \boldsymbol{N} \, dA + \frac{1}{V} \int_{\partial \mathcal{L}_0} \boldsymbol{x} \otimes \boldsymbol{N} \, dA . \tag{23}$$

Furthermore, the volume average of the first Piola-Kirchhoff stress tensor is then given by the surface integrals

$$\frac{1}{V}\int_{\mathcal{B}_0} \boldsymbol{P}\, dV = \frac{1}{V}\int_{\partial\mathcal{B}_0} \boldsymbol{t}_0 \otimes \boldsymbol{X}\, dA + \frac{1}{V}\int_{\partial\mathcal{L}_0} \boldsymbol{t}_0 \otimes \boldsymbol{X}\, dA\,, \tag{24}$$

with $\boldsymbol{t}_0 = \boldsymbol{P}\boldsymbol{N}$ and the outward unit normal $\boldsymbol{N}$. In order to get a simple correlation of the macroscopic quantities in terms of suitable integrals over the $\mathcal{RVE}$ with experimental set-ups, we define the macroscopic deformation gradient and the first Piola-Kirchhoff stress tensor in terms of surface integrals over the boundary $\partial\mathcal{B}_0$ of the $\mathcal{RVE}$:

$$\overline{\boldsymbol{F}} = \frac{1}{V}\int_{\partial\mathcal{B}_0} \boldsymbol{x} \otimes \boldsymbol{N}\, dA\,, \qquad \overline{\boldsymbol{P}} = \frac{1}{V}\int_{\partial\mathcal{B}_0} \boldsymbol{t}_0 \otimes \boldsymbol{X}\, dA\,. \tag{25}$$

By analogy with the previous relations, we obtain

$$\dot{\overline{\boldsymbol{F}}} = \frac{1}{V}\int_{\partial\mathcal{B}_0} \dot{\boldsymbol{x}} \otimes \boldsymbol{N}\, dA\,, \qquad \dot{\overline{\boldsymbol{P}}} = \frac{1}{V}\int_{\partial\mathcal{B}_0} \dot{\boldsymbol{t}}_0 \otimes \boldsymbol{X}\, dA\,. \tag{26}$$

In the following, we neglect holes $\mathcal{L}_0$, then the surface integrals (25, 26) are identical to their volume averages. Similar arguments have to be applied if singular surfaces are taken into account, see e.g. Schröder (2000).

For the following algebraic manipulations we introduce an additive decomposition of the microscopic deformation gradient in a constant and a fluctuation part, i.e.,

$$\boldsymbol{F} = \overline{\boldsymbol{F}} + \widetilde{\boldsymbol{F}}\,. \tag{27}$$

Integration of (27) over the representative volume element yields

$$\overline{\boldsymbol{F}} = \frac{1}{V}\int_{\mathcal{B}_0} \boldsymbol{F}\, dV = \frac{1}{V}\int_{\mathcal{B}_0} (\overline{\boldsymbol{F}} + \widetilde{\boldsymbol{F}})\, dV = \overline{\boldsymbol{F}} + \frac{1}{V}\int_{\mathcal{B}_0} \widetilde{\boldsymbol{F}}\, dV\,. \tag{28}$$

The implication of the latter relation is that the volume averages of the fluctuation part $\widetilde{\boldsymbol{F}}$ vanish, i.e.,

$$\frac{1}{V}\int_{\mathcal{B}_0} \widetilde{\boldsymbol{F}}\, dV = \boldsymbol{0}\,. \tag{29}$$

If we further assume that the fluctuation part of the microscopic deformation gradient can be computed by $\widetilde{\boldsymbol{F}} = \mathrm{Grad}_X \widetilde{\boldsymbol{w}}$, where $\widetilde{\boldsymbol{w}}$ represents the fluctuation part of the deformation field on the micro-scale, then the following condition holds:

$$\frac{1}{V}\int_{\partial\mathcal{B}_0} \widetilde{\boldsymbol{w}} \otimes \boldsymbol{N}\, dA = \boldsymbol{0}\,. \tag{30}$$

By analogy with the decomposition of the microscopic deformation gradient, we introduce an additive decomposition of the microscopic first Piola-Kirchhoff stresses in a constant and a fluctuation part, i.e.,

$$\boldsymbol{P} = \overline{\boldsymbol{P}} + \widetilde{\boldsymbol{P}} \,. \tag{31}$$

The evaluation of the integral of the decomposition (31) over the $\mathcal{RVE}$ yields

$$\overline{\boldsymbol{P}} = \frac{1}{V} \int_{\mathcal{B}_0} \boldsymbol{P} \, dV = \frac{1}{V} \int_{\mathcal{B}_0} (\overline{\boldsymbol{P}} + \widetilde{\boldsymbol{P}}) \, dV = \overline{\boldsymbol{P}} + \frac{1}{V} \int_{\mathcal{B}_0} \widetilde{\boldsymbol{P}} \, dV \,, \tag{32}$$

which implies

$$\frac{1}{V} \int_{\mathcal{B}_0} \widetilde{\boldsymbol{P}} \, dV = \boldsymbol{0} \,. \tag{33}$$

Based on the definition of the traction vector $\boldsymbol{t}_0 = \boldsymbol{P}\boldsymbol{N} = (\overline{\boldsymbol{P}} + \widetilde{\boldsymbol{P}})\boldsymbol{N}$ we introduce the abbreviation $\boldsymbol{t}_0 = \overline{\boldsymbol{t}}_0 + \widetilde{\boldsymbol{t}}_0$ with $\overline{\boldsymbol{t}}_0 = \overline{\boldsymbol{P}}\boldsymbol{N}$ and $\widetilde{\boldsymbol{t}}_0 = \widetilde{\boldsymbol{P}}\boldsymbol{N}$. Inserting these quantities in $(25)_2$ yields

$$\overline{\boldsymbol{P}} = \frac{1}{V} \int_{\partial \mathcal{B}_0} (\overline{\boldsymbol{t}}_0 + \widetilde{\boldsymbol{t}}_0) \otimes \boldsymbol{X} \, dA \,. \tag{34}$$

From one part of the surface integral we derive the relation

$$\frac{1}{V} \int_{\partial \mathcal{B}_0} \overline{\boldsymbol{t}}_0 \otimes \boldsymbol{X} \, dA = \frac{1}{V} \int_{\partial \mathcal{B}_0} (\overline{\boldsymbol{P}}\boldsymbol{N}) \otimes \boldsymbol{X} \, dA = \overline{\boldsymbol{P}} \, \frac{1}{V} \int_{\partial \mathcal{B}_0} \boldsymbol{N} \otimes \boldsymbol{X} \, dA \,, \tag{35}$$

which yields with the relation $\dfrac{1}{V} \displaystyle\int_{\partial \mathcal{B}_0} \boldsymbol{N} \otimes \boldsymbol{X} \, dA = \boldsymbol{1}$ the identity

$$\frac{1}{V} \int_{\partial \mathcal{B}_0} \overline{\boldsymbol{t}}_0 \otimes \boldsymbol{X} \, dA = \overline{\boldsymbol{P}} \,. \tag{36}$$

Therefore, we conclude from (34) that for an equilibrium state

$$\frac{1}{V} \int_{\partial \mathcal{B}_0} \widetilde{\boldsymbol{t}}_0 \otimes \boldsymbol{X} \, dA = \boldsymbol{0} \tag{37}$$

holds. In general, other macroscopic quantities are defined by the standard transformations using the macroscopic stress- and deformation tensors. Thus, the macroscopic Kirchhoff stresses $\overline{\boldsymbol{\tau}}$ are defined as

$$\overline{\boldsymbol{\tau}} = \overline{\boldsymbol{P}} \, \overline{\boldsymbol{F}}^T = \frac{1}{V} \int_{\mathcal{B}_0} \boldsymbol{P} \, dV \quad \left(\frac{1}{V} \int_{\mathcal{B}_0} \boldsymbol{F} \, dV \right)^T \,. \tag{38}$$

In a similar way, we define the macroscopic Cauchy stresses by the transformation

$$\overline{\boldsymbol{\sigma}} = \frac{1}{\overline{J}} \overline{\boldsymbol{P}}\, \overline{\boldsymbol{F}}^T = \frac{1}{\overline{J}} \overline{\boldsymbol{\tau}} = \frac{1}{\overline{J}} \left(\frac{1}{V} \int_{\mathcal{B}_0} \boldsymbol{P}\, dV \right) \left(\frac{1}{V} \int_{\mathcal{B}_0} \boldsymbol{F}\, dV \right)^T . \tag{39}$$

Also the definition of the macroscopic Cauchy-Green tensor is based on the product of the macroscopic deformation gradient, i.e.,

$$\overline{\boldsymbol{C}} = \overline{\boldsymbol{F}}^T \overline{\boldsymbol{F}} = \left(\frac{1}{V} \int_{\mathcal{B}_0} \boldsymbol{F}\, dV \right)^T \left(\frac{1}{V} \int_{\mathcal{B}_0} \boldsymbol{F}\, dV \right) , \tag{40}$$

A simple volume averaging of the microscopic Cauchy-Green tensor

$$\frac{1}{V} \int_{\mathcal{B}_0} \boldsymbol{C}\, dV = \frac{1}{V} \int_{\mathcal{B}_0} \boldsymbol{F}^T \boldsymbol{F}\, dV , \tag{41}$$

leads with the decomposition $\boldsymbol{F} = \overline{\boldsymbol{F}} + \widetilde{\boldsymbol{F}}$ to the expression

$$\begin{aligned} \frac{1}{V} \int_{\mathcal{B}_0} (\overline{\boldsymbol{F}} + \widetilde{\boldsymbol{F}})^T (\overline{\boldsymbol{F}} + \widetilde{\boldsymbol{F}})\, dV = \;& \overline{\boldsymbol{F}}^T \overline{\boldsymbol{F}} + \frac{1}{V} \int_{\mathcal{B}_0} \widetilde{\boldsymbol{F}}^T \widetilde{\boldsymbol{F}}\, dV \\ + \;& \frac{1}{V} \int_{\mathcal{B}_0} (\widetilde{\boldsymbol{F}}^T \overline{\boldsymbol{F}} + \overline{\boldsymbol{F}}^T \widetilde{\boldsymbol{F}})\, dV . \end{aligned} \tag{42}$$

The integral term on the right-hand side

$$\int_{\mathcal{B}_0} (\widetilde{\boldsymbol{F}}^T \overline{\boldsymbol{F}} + \overline{\boldsymbol{F}}^T \widetilde{\boldsymbol{F}})\, dV = \int_{\mathcal{B}_0} \widetilde{\boldsymbol{F}}^T\, dV\, \overline{\boldsymbol{F}} + \overline{\boldsymbol{F}}^T \int_{\mathcal{B}_0} \widetilde{\boldsymbol{F}}\, dV \tag{43}$$

vanishes obviously, thus the remaining expression of (41) is

$$\frac{1}{V} \int_{\mathcal{B}_0} \boldsymbol{C}\, dV = \overline{\boldsymbol{F}}^T \overline{\boldsymbol{F}} + \frac{1}{V} \int_{\mathcal{B}_0} \widetilde{\boldsymbol{F}}^T \widetilde{\boldsymbol{F}}\, dV , \tag{44}$$

which differs from (40) by the integral term on the right-hand side in (44).

Equivalences between the definitions (38) and (39) and direct averages of $\boldsymbol{\tau}$ and $\boldsymbol{\sigma}$ with respect to the volume of the $\mathcal{RVE}$ in the reference and actual placement, respectively, i.e.

$$\overline{\boldsymbol{\tau}} \equiv \frac{1}{V} \int_{\mathcal{B}_0} \boldsymbol{\tau}\, dV , \qquad \overline{\boldsymbol{\sigma}} \equiv \frac{1}{v} \int_{\mathcal{B}_t} \boldsymbol{\sigma}\, dv \tag{45}$$

hold only for specific boundary conditions and geometries, see e.g. de Souza Neto and Feijoo (2008). If the conditions are satisfied, we obtain for the Kirchhoff stresses and by analogy for the Cauchy stresses, assuming (19):

$$\frac{1}{V} \int_{\mathcal{B}_0} \boldsymbol{\tau}\, dV = \frac{1}{V} \int_{\partial \mathcal{B}_0} \boldsymbol{t}_0 \otimes \boldsymbol{x}\, dA , \qquad \frac{1}{v} \int_{\mathcal{B}_t} \boldsymbol{\sigma}\, dv = \frac{1}{v} \int_{\partial \mathcal{B}_t} \boldsymbol{t} \otimes \boldsymbol{x}\, da \tag{46}$$

with $\boldsymbol{t} = \boldsymbol{\sigma}\boldsymbol{n}$ and the outward unit normal $\boldsymbol{n}$ on $\partial\mathcal{B}_t$. Useful relations for further kinematical quantities and stress measures in finite deformation plasticity are given in Nemat-Nasser (1999); for the elastoplasticity of polycrystals see Clayton and McDowell (2003).

2.4 Macro-homogeneity condition

One of the most important relations in micro-macro transition schemes is the *macro-homogeneity condition* (also denoted as Hill's condition or Hill-Mandel condition), Hill (1965a) and Mandel (1972). In the finite strain setting, we define the condition as

$$\overline{\boldsymbol{P}} : \dot{\overline{\boldsymbol{F}}} = \frac{1}{V} \int_{\partial\mathcal{B}_0} \boldsymbol{t}_0 \cdot \dot{\boldsymbol{x}} \, dA \,, \tag{47}$$

which leads with the algebraic manipulations

$$\frac{1}{V} \int_{\partial\mathcal{B}_0} \boldsymbol{t}_0 \cdot \dot{\boldsymbol{x}} \, dA = \frac{1}{V} \int_{\partial\mathcal{B}_0} (\boldsymbol{P}\boldsymbol{N}) \cdot \dot{\boldsymbol{x}} \, dA = \frac{1}{V} \int_{\partial\mathcal{B}_0} \boldsymbol{P} : \dot{\boldsymbol{x}} \otimes \boldsymbol{N} \, dA$$

and the application of the Gaussian integral theorem

$$\int_{\partial\mathcal{B}_0} \boldsymbol{P} : \dot{\boldsymbol{x}} \otimes \boldsymbol{N} \, dA = \int_{\mathcal{B}_0} \mathrm{Div}_X [\dot{\boldsymbol{x}}\boldsymbol{P}] \, dV = \int_{\mathcal{B}_0} (\boldsymbol{P} : \mathrm{Grad}_X \dot{\boldsymbol{x}} + \dot{\boldsymbol{x}} \mathrm{Div}_X \boldsymbol{P}) \, dV$$

and taking into account the equilibrium condition (19) to the volume average

$$\overline{\boldsymbol{P}} : \dot{\overline{\boldsymbol{F}}} = \frac{1}{V} \int_{\mathcal{B}_0} \boldsymbol{P} : \dot{\boldsymbol{F}} \, dV \,, \tag{48}$$

with $\dot{\boldsymbol{F}} = \mathrm{Grad}_X \dot{\boldsymbol{x}}$. It should be noted that the macro-homogeneity condition of Hill and Mandel is written as the volume average of the scalar product of first Piola-Kirchhoff stresses and the deformation gradient with respect to the parametrization of the $\mathcal{RVE}$ in the reference placement.

2.5 Constraint/Boundary conditions on the micro-scale

Following the explanations of Hill (1984), we write the identity

$$\frac{1}{V} \int_{\mathcal{B}_0} \boldsymbol{P} : \dot{\boldsymbol{F}} \, dV - \overline{\boldsymbol{P}} : \dot{\overline{\boldsymbol{F}}} = \frac{1}{V} \int_{\mathcal{B}_0} ((\boldsymbol{P} - \overline{\boldsymbol{P}}) : (\dot{\boldsymbol{F}} - \dot{\overline{\boldsymbol{F}}})) \, dV \,. \tag{49}$$

If the right-hand side of the latter equation vanishes, the theorem of product averages (48) is satisfied. Two simple solutions are obtained by setting

$$\boldsymbol{P} = \overline{\boldsymbol{P}} \quad \forall \boldsymbol{X} \in \mathcal{B}_0 \quad \text{or} \quad \dot{\boldsymbol{F}} = \dot{\overline{\boldsymbol{F}}} \quad \forall \boldsymbol{X} \in \mathcal{B}_0 \,, \tag{50}$$

where the first assumption of constant stresses over the $\mathcal{RVE}$ is associated to the estimate of Reuss and the second of a constant deformation gradient to the estimate of Voigt. In the following, we denote the implications in (50) as constraint conditions.

Let us now consider the right-hand side of (49); with the definition of the microscopic deformation gradient (13) and the relation $\mathrm{Grad}_X \boldsymbol{X} = \mathbf{1}$, we obtain

$$\int_{\mathcal{B}_0} (\boldsymbol{P} - \overline{\boldsymbol{P}}) : (\mathrm{Grad}_X \dot{\boldsymbol{x}} - \dot{\overline{\boldsymbol{F}}}\, \mathrm{Grad}_X \boldsymbol{X})\, dV\,. \tag{51}$$

With the equilibrium requirement $\mathrm{Div}_X(\boldsymbol{P} - \overline{\boldsymbol{P}}) = \mathbf{0}$ and the Cauchy theorem $\boldsymbol{t}_0 = \boldsymbol{P}\boldsymbol{N}$, we derive the following equivalent expression of (48):

$$\int_{\partial\mathcal{B}_0} (\boldsymbol{t}_0 - \overline{\boldsymbol{P}}\boldsymbol{N}) \cdot (\dot{\boldsymbol{x}} - \dot{\overline{\boldsymbol{F}}}\boldsymbol{X})\, dA = 0\,. \tag{52}$$

The above relations do not only hold for $\mathrm{Grad}_X \dot{\boldsymbol{x}} = \dot{\boldsymbol{F}}$, but also for $\delta\boldsymbol{F}$ as well as for $\boldsymbol{F}$, etc.; therefore, we can replace $\dot{\overline{\boldsymbol{F}}}$ by $\delta\overline{\boldsymbol{F}}$ and $\overline{\boldsymbol{F}}$. *Dirichlet boundary conditions* are defined by setting the second bracket term in (52) equal to zero, it follows

$$\boldsymbol{x} = \overline{\boldsymbol{F}}\boldsymbol{X} \quad \forall \boldsymbol{X} \in \partial\mathcal{B}_0\,. \tag{53}$$

Analogously, enforcing the first bracket term in (52) to be zero yields the *Neumann boundary conditions*

$$\boldsymbol{t}_0 = \overline{\boldsymbol{P}}\boldsymbol{N} \quad \forall \boldsymbol{X} \in \partial\mathcal{B}_0\,. \tag{54}$$

For the derivation of *periodic boundary conditions* we decompose the boundary of the microstructure ∂B_0 into two associated parts

$$\partial\mathcal{B}_0 = \partial\mathcal{B}_0^- \cup \partial\mathcal{B}_0^+\,. \tag{55}$$

Every point $\boldsymbol{X}^+ \in \partial\mathcal{B}^+$ is assumed to have an associated point $\boldsymbol{X}^- \in \partial\mathcal{B}^-$ with outward unit normals $\boldsymbol{N}^+$ and $\boldsymbol{N}^-$, respectively. Since $\overline{\boldsymbol{F}}$ as well as $\boldsymbol{X}$ are assumed to be given quantities, we define the fluctuation field

$$\widetilde{\boldsymbol{w}} := \boldsymbol{x} - \overline{\boldsymbol{F}}\boldsymbol{X}\,. \tag{56}$$

Thus, the macro-homogeneity condition (52) appears as

$$\begin{aligned}\int_{\partial\mathcal{B}_0} (\boldsymbol{t}_0 - \overline{\boldsymbol{P}}\boldsymbol{N}) \cdot \widetilde{\boldsymbol{w}}\, dA = &\int_{\partial\mathcal{B}_0^+} (\boldsymbol{t}_0^+ - \overline{\boldsymbol{P}}\boldsymbol{N}^+) \cdot \widetilde{\boldsymbol{w}}^+\, dA \\ &+ \int_{\partial\mathcal{B}_0^-} (\boldsymbol{t}_0^- - \overline{\boldsymbol{P}}\boldsymbol{N}^-) \cdot \widetilde{\boldsymbol{w}}^-\, dA\,.\end{aligned} \tag{57}$$

Table 1. constraint conditions & boundary conditions (bcs)

Reuss	$\boldsymbol{P} = \overline{\boldsymbol{P}}$	$\forall \boldsymbol{X} \in \mathcal{B}_0$
Voigt	$\boldsymbol{F} = \overline{\boldsymbol{F}}$	$\forall \boldsymbol{X} \in \mathcal{B}_0$
Dirichlet bcs	$\boldsymbol{x} = \overline{\boldsymbol{F}}\boldsymbol{X}$	$\forall \boldsymbol{X} \in \partial\mathcal{B}_0$
Neumann bcs	$\boldsymbol{t}_0 = \overline{\boldsymbol{P}}\boldsymbol{N}$	$\forall \boldsymbol{X} \in \partial\mathcal{B}_0$
periodic bcs	$\widetilde{\boldsymbol{w}} = \boldsymbol{x} - \overline{\boldsymbol{F}}\boldsymbol{X}$ $\widetilde{\boldsymbol{w}}^+ = \widetilde{\boldsymbol{w}}^-$ $\boldsymbol{t}_0^+ = -\boldsymbol{t}_0^-$	$\forall \boldsymbol{X}^+ \in \partial\mathcal{B}_0^+$ and $\boldsymbol{X}^- \in \partial\mathcal{B}_0^-$

A periodic fluctuation field is characterized by $\widetilde{\boldsymbol{w}}^+ = \widetilde{\boldsymbol{w}}^-$ at associated points, with the essential requirement $\boldsymbol{N}^+ = -\boldsymbol{N}^-$ it follows

$$\int_{\partial\mathcal{B}_0^+} \left\{ (\boldsymbol{t}_0^+ - \overline{\boldsymbol{P}}\boldsymbol{N}^+) \cdot \widetilde{\boldsymbol{w}}^+ + (\boldsymbol{t}_0^- + \overline{\boldsymbol{P}}\boldsymbol{N}^+) \cdot \widetilde{\boldsymbol{w}}^+ \right\} dA = \int_{\partial\mathcal{B}_0^+} (\boldsymbol{t}_0^+ + \boldsymbol{t}_0^-) \cdot \widetilde{\boldsymbol{w}}^+ \, dA \,. \tag{58}$$

The latter expression is identical to zero if $\boldsymbol{t}_0^+ = -\boldsymbol{t}_0^-$ holds.

An appropriate requirement for the type of the boundary condition to be used can be rephrased as follows

- Suquet (1987): *"The boundary conditions must reproduce, as closely as possible, the in situ state of the $\mathcal{RVE}$ inside the material".*

It should be noted that linear boundary displacements yield an energetically upper bound, whereas uniform boundary tractions provide a lower bound of the homogenized system. Nevertheless, the choice of the boundary condition influences the mechanical response in many cases:

- Xia et al. (2003): *"... 'homogeneous boundary conditions' are not only over-constrained but they may also violate the boundary traction periodicity conditions.".*

For periodic media, a natural course of action are periodic boundary conditions. They can be realized in a *strong format*, i.e., one part of the discretized boundary of the $\mathcal{RVE}$ (the *image boundary*, e.g. $\partial\mathcal{B}_0^-$) must be completely mirrored to the nodes on the associated part of the boundary (the *mirror boundary* $\partial\mathcal{B}_0^+$). Alternatively, a *weak format* of the periodic boundary conditions is proposed in Larsson et al. (2011). In this context, we also refer to Miehe and Bayreuther (2007).

In order to discuss the influence of the different boundary conditions on the mechanical response, we consider a periodic microstructure with stiff inclusions embedded in a weak matrix, as shown in Fig. 4a.

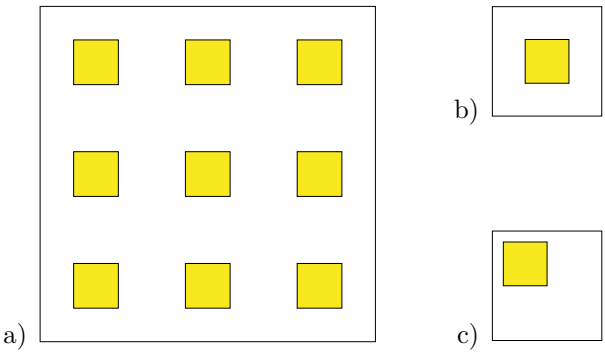

Figure 4. Periodic microstructure: a) Continuous matrix with periodically distributed inclusions. $\mathcal{RVE}s$ with b) a centric and c) an eccentric inclusion, see Schröder (2000).

For the analysis we choose unit cells which are discretized with 20×20 equal-sized quadrilateral elements, the inclusion is discretized with 8×8 elements. We choose a unit cell with a centric inclusion, as depicted in Fig. 4b and one unit cell with an eccentric inclusion, cf. Fig. 4c. The simulation is carried out for small strains under plain strain conditions and we apply an isotropic constitutive law for both, the weak matrix and the stiffer inclusion material. As mentioned above, for the considered periodic media the natural choice are periodic boundary conditions. That means, that for both unit cells, cf. Fig. 4b,c, the periodic boundary conditions must yield identical results. For the macroscopic loading

$$\overline{\boldsymbol{F}} = \text{diag}[\, 1.0005 \,;\; 1.0 \,;\; 1.0 \,]\,, \tag{59}$$

we obtain the stress distribution as depicted in Fig. 5. In both cases, the macroscopic Cauchy stress tensor has only non-vanishing and identical diagonal components, as expected; the values of the components of the stress tensor (in consistent units) are

$$\overline{\boldsymbol{\sigma}}^{per} = \text{diag}[\, 837.4 \,;\; 490.7 \,;\; 530.7 \,]\,. \tag{60}$$

These stress values will be applied to the unit cells when we analyze the Neumann boundary conditions. The stress response for the Dirichlet boundary conditions is depicted in Fig. 6. For the unit cell with centered inclusion, the macroscopic stress tensor is also diagonal and the values differ

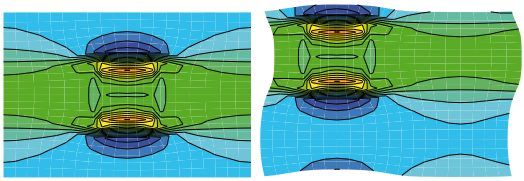

Figure 5. Stress σ_{11} in the unit cells with centric (left) and eccentric (right) inclusion under periodic boundary conditions, see Schröder (2000).

approximately by 1% compared to (60) and the local stress distribution is comparable to the ones in Fig. 5. Considering the unit cell with the eccentric inclusion, we observe a symmetry-break in the stress distribution. Nevertheless, the stress components deviate from the components in (60) by approx. 3%, in addition the off-diagonal element of $\overline{\boldsymbol{\sigma}}$ is not vanishing.

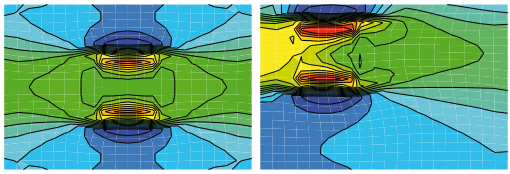

Figure 6. Stress σ_{11} in the unit cells with centric (left) and eccentric (right) inclusion under Dirichlet boundary conditions, see Schröder (2000).

Applying the stress values of (60) as loading conditions for the Neumann boundary conditions, we get the results shown in Fig. 7. The macroscopic deformation gradient should be close to (59). The deviation for both unit cells is approximately up to 8% and again we observe a symmetry-break in the local stress distribution for the unit cell with the eccentric inclusion.
Sum up: As expected, periodic boundary conditions yield the best results.

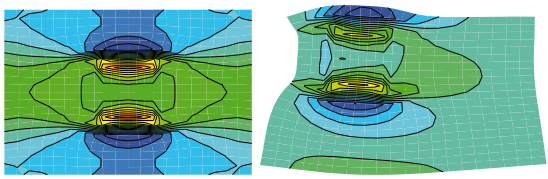

Figure 7. Stress σ_{11} in the unit cells with centric (left) and eccentric (right) inclusion under Neumann boundary conditions, see Schröder (2000).

2.6 Remarks on the Choice of the $\mathcal{RVE}$

The choice of the representative volume element ($\mathcal{RVE}$) for the application to a two-scale homogenization scheme is an ongoing research topic. In general, the $\mathcal{RVE}$ should be a partial volume of the material, which is statistically homogeneous from the macroscopic point of view. Furthermore, the choice of a $\mathcal{RVE}$ is not unique, see Fig. 8.

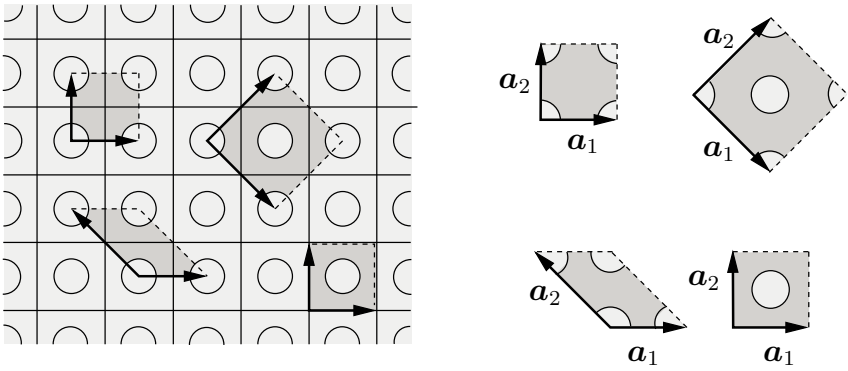

Figure 8. Non-uniqueness of the $\mathcal{RVE}$s of a periodically arranged microstructure. The dashed boxed regions represent four possible $\mathcal{RVE}$s, see Schröder (2000).

In Zeman (2003), several properties for the definition of a $\mathcal{RVE}$, taken from the literature, are summarized:

- Hill (1963): *"This phrase (the $\mathcal{RVE}$) will be used when referring to a sample that (a) is structurally entirely typical of the whole structure on average, and (b) contains sufficient number of inclusions for the apparent overall moduli to be effectively independent of the surface value of traction and displacement, so long as these values are "macroscopically uniform""*

- Hashin (1983): *"The RVE is a model of the material to be used to determine the corresponding effective properties of the homogenized macroscopic model. The RVE should be large enough to contain sufficient information about the microstructure in order to be representative, however it should be much smaller than the macroscopic body."*

- Drugan and Willis (1996): *"The RVE is the smallest material volume element of the composite for which the usual spatially constant "over-*

all modulus" macroscopic constitutive representation is a sufficiently accurate model to represent the mean constitutive response."

- Ostoja-Starzewski (2001): *"The RVE is very clearly defined in two situations only: (i) it is a unit cell of a periodic microstructure, and (ii) volume containing a very large set of micro-scale elements, possessing statistically homogeneous and ergodic properties."*

- Stroeven et al. (2002): *"The determination of the RVE size is by no means straightforward. It depends on the material under consideration, but also on the structure sensitivity of the physical quantity that is measured. Normally, elastic moduli are taken as the governing parameter, however, other quantities can also be taken, such as energy dissipation in case of microstructural cracking."*

A note on periodic unit cells: In periodic media, typically unit cells, which are translationally symmetric, are used as $\mathcal{RVE}$s. In order to design (sub-) unit cells with a lower number of degrees of freedom, Ohno et al. (2001) exploited the point symmetrical distribution of the mechanical field quantities with respect to the center of the considered unit cell. Substantial savings in computer time can also be realized when the unit cell possesses further special symmetries, see Flores and de Souza Neto (2010).

A note on random microstructures: Capturing the random nature of microstructures is a challenge in homogenization (effective macroscopic description). The lack of microstructural periodicity implies that we have to analyze statistical volume elements ($\mathcal{SVE}s$) instead of $\mathcal{RVE}s$. Mathematical tools for the characterization of random microstructures are discussed in Ohser and Mücklich (2000). A brief introduction of basic morphological measurements for a quantitative characterization of the geometry of random microstructures is given in Jeulin and Ostoja-Starzewski (2001). From the viewpoint of stochastical mechanics, we could consider ensemble averages over several realizations of the microstructure. From the practical point of view, we are interested in only one realization of the microstructure in order to achieve a sufficient estimate of the macroscopic mechanical response. Furthermore, the interchangeability of the ensemble averaging and volume averaging (in general for sufficiently large microstructures) is a key assumption in this field, which is based on the concepts of statistical homogeneity and ergodicity, see Jeulin and Ostoja-Starzewski (2001) and Ostoja-Starzweski (2008).

3 Algorithmic Treatment

This chapter concerns the theoretical and numerical treatment of a discrete two-scale homogenization scheme, also known as the FE^2-method or direct micro-macro transition approach. A major role plays the coupled numerical solution of the boundary value problems on both scales. Especially the consistent linearization of the effective macroscopic response function can be seen as a crucial part in this numerical scheme. In the following, the (matrix) approximations of the field quantities are denoted by a superscript h, e.g., the discrete counterpart of $\boldsymbol{x}$ is denoted as $\boldsymbol{x}^h$.

3.1 Boundary Value Problems on the Macro- and Micro-Scale

The *balance of linear momentum at the macro-scale* (11) can be written in its weak form as

$$\overline{G} = -\int_{\overline{\mathcal{B}}_0} \delta\overline{\boldsymbol{x}} \cdot \left(\mathrm{Div}_{\overline{X}}\overline{\boldsymbol{P}} + \overline{\boldsymbol{f}}\right) \, dV \tag{61}$$

with $\overline{G} = 0$ at the equilibrium state. Application of the relation

$$\delta\overline{\boldsymbol{x}} \cdot \mathrm{Div}_{\overline{X}}\,\overline{\boldsymbol{P}} = \mathrm{Div}_{\overline{X}}[\delta\overline{\boldsymbol{x}}\,\overline{\boldsymbol{P}}] - \mathrm{Grad}_{\overline{X}}\delta\overline{\boldsymbol{x}} : \overline{\boldsymbol{P}} \tag{62}$$

and the Gauss integral theorem yields the modified expression

$$\overline{G} = \underbrace{\int_{\overline{\mathcal{B}}_0} \delta\overline{\boldsymbol{F}} : \overline{\boldsymbol{P}} \, dV}_{=:\,\overline{G}^{int}} - \underbrace{\left\{ \int_{\overline{\mathcal{B}}_0} \delta\overline{\boldsymbol{x}} \cdot \overline{\boldsymbol{f}} \, dV + \int_{\partial\overline{\mathcal{B}}_0} \delta\overline{\boldsymbol{x}} \cdot \overline{\boldsymbol{t}}_0 \, dA \right\}}_{=:\,\overline{G}^{ext}} \tag{63}$$

with $\overline{\boldsymbol{t}}_0 = \overline{\boldsymbol{P}}\,\overline{\boldsymbol{N}}$. For the discretization of the *macroscopic boundary value problem*, we apply the following discretizations for the actual, virtual and incremental deformation within a typical finite element

$$\overline{\boldsymbol{x}}^h = \overline{\boldsymbol{X}}^h + \mathbb{N}^e\overline{\boldsymbol{d}}\,, \quad \delta\overline{\boldsymbol{x}}^h = \mathbb{N}^e\delta\overline{\boldsymbol{d}}\,, \qquad \Delta\overline{\boldsymbol{x}}^h = \mathbb{N}^e\Delta\overline{\boldsymbol{d}}\,, \tag{64}$$

respectively. Here the matrix $\mathbb{N}^e$ contains the classical ansatz-functions and the vectors $\{\overline{\boldsymbol{d}}\,, \delta\overline{\boldsymbol{d}}\,, \Delta\overline{\boldsymbol{d}}\}$ represent the actual, virtual and incremental nodal displacements. With the $\mathbb{B}^e$-matrices containing the partial derivatives of the ansatz functions with respect to reference coordinates, we define the approximations of the actual, virtual and incremental deformation tensors

$$\overline{\boldsymbol{F}}^h = \mathbf{1}^h + \mathbb{B}^e\overline{\boldsymbol{d}}\,, \qquad \delta\overline{\boldsymbol{F}}^h = \mathbb{B}^e\delta\overline{\boldsymbol{d}}\,, \qquad \Delta\overline{\boldsymbol{F}}^h = \mathbb{B}^e\Delta\overline{\boldsymbol{d}}\,. \tag{65}$$

Inserting the approximations for the virtual fields (64) and (65) in Eq. (63) yields the approximation of $\overline{G}(\overline{\boldsymbol{x}}, \delta\overline{\boldsymbol{x}})$ by $\overline{G}^h(\overline{\boldsymbol{x}}^h, \delta\overline{\boldsymbol{x}}^h)$, i.e.

$$\overline{G}^h = \sum_e \overline{G}^e(\overline{\boldsymbol{x}}^h, \delta\overline{\boldsymbol{x}}^h) = \sum_e \overline{G}^{e,int}(\overline{\boldsymbol{x}}^h, \delta\overline{\boldsymbol{x}}^h) - \sum_e \overline{G}^{e,ext}(\overline{\boldsymbol{x}}^h, \delta\overline{\boldsymbol{x}}^h) \,. \quad (66)$$

If the weak form (63) is associated with a typical finite element, we get the expressions for the internal and external parts

$$\overline{G}^{e,int}(\overline{\boldsymbol{x}}^h, \delta\overline{\boldsymbol{x}}^h) = \delta\overline{\boldsymbol{d}}^T \underbrace{\int_{\overline{\mathcal{B}}_0^e} \mathbb{B}^{eT} \overline{\boldsymbol{P}}^h \, dV}_{=:\,\overline{\boldsymbol{r}}^{e,int}} \,, \quad (67)$$

and

$$\overline{G}^{e,ext}(\overline{\boldsymbol{x}}^h, \delta\overline{\boldsymbol{x}}^h) = \delta\overline{\boldsymbol{d}}^T \underbrace{\left\{ \int_{\overline{\mathcal{B}}_0^e} \mathbb{N}^e \overline{\boldsymbol{f}}^h \, dV + \int_{\partial\overline{\mathcal{B}}_0^e} \mathbb{N}^e \overline{\boldsymbol{t}}_0^h \, dA \right\}}_{=:\,\overline{\boldsymbol{r}}^{e,ext}} \,. \quad (68)$$

With this, the element residual vector $\overline{\boldsymbol{r}}^e$ is computed by $\overline{\boldsymbol{r}}^e = \overline{\boldsymbol{r}}^{e,int} - \overline{\boldsymbol{r}}^{e,ext}$. To solve the nonlinear weak form $\overline{G}^h(\overline{\boldsymbol{x}}^h, \delta\overline{\boldsymbol{x}}^h)$ we apply the Newton-Raphson iteration scheme. Therefore, the linerization of $\overline{G}^h(\overline{\boldsymbol{x}}^h, \delta\overline{\boldsymbol{x}}^h)$ at $\overline{\boldsymbol{x}}^h = \overline{\boldsymbol{x}}^{h*}$ has to be computed:

$$\mathrm{Lin}\, \overline{G}^h(\overline{\boldsymbol{x}}^{h*}, \delta\overline{\boldsymbol{x}}^h, \Delta\overline{\boldsymbol{x}}^h) = \overline{G}^h(\overline{\boldsymbol{x}}^{h*}, \delta\overline{\boldsymbol{x}}^h) + \Delta\overline{G}^h(\overline{\boldsymbol{x}}^{h*}, \delta\overline{\boldsymbol{x}}^h, \Delta\overline{\boldsymbol{x}}^h) \,. \quad (69)$$

The linear increment is defined as the directional derivative of $\overline{G}^h$ at $\overline{\boldsymbol{x}}^h$ in the direction of the incremental deformation $\Delta\overline{\boldsymbol{x}}^h$, i.e.,

$$\Delta\overline{G}^h(\overline{\boldsymbol{x}}^{h*}, \delta\overline{\boldsymbol{x}}^h, \Delta\overline{\boldsymbol{x}}^h) = \frac{d}{d\epsilon} \left[\overline{G}^h(\overline{\boldsymbol{x}}^{h*} + \epsilon\Delta\overline{\boldsymbol{x}}^h, \delta\overline{\boldsymbol{x}}^h) \right] \Big|_{\epsilon=0} \,. \quad (70)$$

For dead-loaded systems the linear increment of the discrete form of $\overline{G}$ is formally given by

$$\Delta\overline{G}^h = \sum_e \Delta\overline{G}^{e,int} \quad (71)$$

and the linear increment for a typical element is calculated by

$$\Delta\overline{G}^{e,int} = \int_{\overline{\mathcal{B}}_0^e} \delta\overline{\boldsymbol{F}}^{hT} \overline{\mathbb{A}}^h \Delta\overline{\boldsymbol{F}}^h \, dV = \delta\overline{\boldsymbol{d}}^T \underbrace{\int_{\overline{\mathcal{B}}_0^e} \mathbb{B}^{eT} \overline{\mathbb{A}}^h \mathbb{B}^e \, dV}_{=:\,\overline{\boldsymbol{k}}^e} \Delta\overline{\boldsymbol{d}} \,. \quad (72)$$

For the computation of the stiffness matrix $\overline{\boldsymbol{k}}^e$ for a macroscopic element, we need the macroscopic (overall) algorithmic consistent moduli $\overline{\mathbb{A}}$, which is formally defined by the partial derivative

$$\overline{\mathbb{A}} = \frac{\partial \overline{\boldsymbol{P}}}{\partial \overline{\boldsymbol{F}}} \quad \text{with} \quad \overline{\boldsymbol{P}} = \frac{1}{V} \int_{\mathcal{B}_0} \boldsymbol{P}(\boldsymbol{F})\, dV \ . \tag{73}$$

This fourth-order tensor cannot be computed directly, becauce we have no explicit expression of the macroscopic first Piola-Kirchhoff stress tensor $\overline{\boldsymbol{P}}$ as a function of its work-conjugated variable, the macroscopic deformation gradient $\overline{\boldsymbol{F}}$. An efficient algorithmic treatment of handling this is presented in the next chapter; therefore, we assume the algorithmic consistent moduli $\overline{\mathbb{A}}$ as known at this point. Thus, the linearization yields

$$\sum_{e=1}^{\overline{num}_{ele}} \left\{ \delta \overline{\boldsymbol{d}}^T \left(\overline{\boldsymbol{k}}^e \Delta \overline{\boldsymbol{d}} + \overline{\boldsymbol{r}}^e \right) \right\} = 0 \ , \tag{74}$$

where $\overline{num}_{ele}$ denotes the number of macroscopic finite elements. The application of the assembling procedure yields the system of equations

$$\overline{\boldsymbol{K}} \Delta \overline{\boldsymbol{D}} = -\overline{\boldsymbol{R}} \quad \text{with} \quad \overline{\boldsymbol{K}} = \mathop{\mathsf{A}}_{e=1}^{\overline{num}_{ele}} \overline{\boldsymbol{k}}^e \quad \text{and} \quad \overline{\boldsymbol{R}} = \mathop{\mathsf{A}}_{e=1}^{\overline{num}_{ele}} \overline{\boldsymbol{r}}^e \, , \tag{75}$$

where A denote the standard assembling operators. The solution of the latter system of equations yields an increment of the actual deformation field. This procedure has to be repeated until an equilibrium state of the macroscopic boundary value problem has been reached, i.e. $\overline{G}^h(\overline{\boldsymbol{x}}, \delta \overline{\boldsymbol{x}}) \approx 0$.

The weak form of the *balance of linear momentum at the microscale*, based on the expression $(19)_1$, is given by

$$G = -\int_{\mathcal{B}_0} \delta \boldsymbol{x} \cdot \mathrm{Div}_X \boldsymbol{P}\, dV \tag{76}$$

with $G = 0$. Here, we are neglecting the volume acceleration and inertia terms. Taking into account the additive split of the deformation into a linear map $\overline{\boldsymbol{F}}\boldsymbol{X}$ and a fluctuation part $\widetilde{\boldsymbol{w}}$, we obtain the following representation of the microscopic deformation tensor $\boldsymbol{F} = \mathrm{Grad}_X \boldsymbol{x}$:

$$\boldsymbol{F} = \overline{\boldsymbol{F}} + \widetilde{\boldsymbol{F}} \quad \text{with} \quad \widetilde{\boldsymbol{F}} = \mathrm{Grad}_X \widetilde{\boldsymbol{w}} \ . \tag{77}$$

With this in hand, we get the modified expression

$$G = \int_{\mathcal{B}_0} \delta \widetilde{\boldsymbol{F}} : \boldsymbol{P}\, dV \ . \tag{78}$$

Note that the part $\overline{\boldsymbol{F}}$ of the microscopic deformation gradient $\boldsymbol{F}$ is given and constant over the $\mathcal{RVE}$.

For the discretization of the *microscopic boundary value problem*, we apply the following discretizations for the actual, virtual and incremental fluctuation within a typical finite element

$$\widetilde{\boldsymbol{w}}^h = \mathbb{N}^e \widetilde{\boldsymbol{d}}, \qquad \delta\widetilde{\boldsymbol{w}}^h = \mathbb{N}^e \delta\widetilde{\boldsymbol{d}}, \qquad \Delta\widetilde{\boldsymbol{w}}^h = \mathbb{N}^e \Delta\widetilde{\boldsymbol{d}}, \tag{79}$$

respectively. Here, the matrix $\mathbb{N}^e$ contains the classical ansatz-functions and the vectors $\{\widetilde{\boldsymbol{d}}, \delta\widetilde{\boldsymbol{d}}, \Delta\widetilde{\boldsymbol{d}}\}$ represent the actual, virtual and incremental nodal fluctuations. With the $\mathbb{B}^e$-matrices containing the partial derivatives of the ansatz functions with respect to reference coordinates, we define the approximations of the actual, virtual and incremental deformation tensors

$$\widetilde{\boldsymbol{F}}^h = \mathbb{B}^e \widetilde{\boldsymbol{d}}, \qquad \delta\widetilde{\boldsymbol{F}}^h = \mathbb{B}^e \delta\widetilde{\boldsymbol{d}}, \qquad \Delta\widetilde{\boldsymbol{F}}^h = \mathbb{B}^e \Delta\widetilde{\boldsymbol{d}}\,. \tag{80}$$

Inserting the approximations for the virtual fields (79) and (80) in (78) leads to the discrete counterpart G^h of G:

$$G^h(\boldsymbol{x}^h, \delta\boldsymbol{x}^h) = \sum_e G^e(\boldsymbol{x}^h, \delta\boldsymbol{x}^h) \tag{81}$$

with

$$G^e(\boldsymbol{x}^h, \delta\boldsymbol{x}^h) = \delta\boldsymbol{d}^T \underbrace{\int_{\mathcal{B}_0^e} \mathbb{B}^{eT} \boldsymbol{P}^h \, dV}_{=:\,\boldsymbol{r}^e}\,. \tag{82}$$

To solve the nonlinear discrete weak form $G^h(\boldsymbol{x}^h, \delta\boldsymbol{x}^h)$, we apply the Newton-Raphson iteration scheme and apply the linerization analogously to the procedure at the macro-scale described above. Finally, we obtain the linear increment for a typical microscopic finite element

$$\Delta G^e = \int_{\mathcal{B}_0^e} \delta\widetilde{\boldsymbol{F}}^{h\,T} \mathbb{A}^h \Delta\widetilde{\boldsymbol{F}}^h \, dV = \delta\widetilde{\boldsymbol{d}}^T \underbrace{\int_{\mathcal{B}_0^e} \mathbb{B}^{eT} \mathbb{A}^h \mathbb{B}^e \, dV}_{=:\,\boldsymbol{k}^e} \Delta\widetilde{\boldsymbol{d}}\,. \tag{83}$$

The application of the standard assembling operator, cf. Eq. (75), to the microscopic stiffness matrices and the residual vectors result in the system of equations

$$\boldsymbol{K}\Delta\widetilde{\boldsymbol{D}} + \boldsymbol{R} = 0\,. \tag{84}$$

From this system of equations, we obtain an update of the discrete fluctuation field and evaluate the discrete weak form (82). If the euclidian norm of $\boldsymbol{R}$ is higher than a given tolerance, we apply further Newton iteration steps until convergence is achieved.

3.2 Computation of Algorithmic Consistent Overall Moduli

In the previous section, we assumed that the macroscopic overall moduli $\overline{\mathbb{A}}$ was given during the solution process at the macro-scale. However, in contrast to the macroscopic stress tensor $\overline{\boldsymbol{P}}$, which can be calculated directly as the volume average of the microscopic counterparts, the macroscopic moduli cannot be consistently computed solely by volumetric averaging. Starting from the incremental constitutive relation at the macro-scale

$$\Delta\overline{\boldsymbol{P}} = \left\{ \frac{1}{V} \frac{\partial}{\partial \overline{\boldsymbol{F}}} \int_{\mathcal{B}} \boldsymbol{P}(\boldsymbol{F})\, dV \right\} : \Delta\overline{\boldsymbol{F}} =: \overline{\mathbb{A}} : \Delta\overline{\boldsymbol{F}} \,, \tag{85}$$

we define the overall (effective) nominal moduli as follows

$$\overline{\mathbb{A}} = \frac{1}{V} \int_{\mathcal{B}} \frac{\partial}{\partial \overline{\boldsymbol{F}}} \boldsymbol{P}(\boldsymbol{F})\, dV = \frac{1}{V} \int_{\mathcal{B}} \frac{\partial \boldsymbol{P}(\boldsymbol{F})}{\partial \boldsymbol{F}} : \frac{\partial \boldsymbol{F}}{\partial \overline{\boldsymbol{F}}}\, dV \,. \tag{86}$$

Let us now exploit the additive decomposition of $\boldsymbol{F}$ into a constant and a fluctuating part. Substituting

$$\boldsymbol{F} = \overline{\boldsymbol{F}} + \widetilde{\boldsymbol{F}} \,, \tag{87}$$

in Equation (86) yields

$$\overline{\mathbb{A}} = \frac{1}{V} \int_{\mathcal{B}} \frac{\partial \boldsymbol{P}(\boldsymbol{F})}{\partial \boldsymbol{F}} : \frac{\partial (\overline{\boldsymbol{F}} + \widetilde{\boldsymbol{F}})}{\partial \overline{\boldsymbol{F}}}\, dV \,. \tag{88}$$

Thus, we obtain with the abbreviation $\mathbb{A} := \partial_F \boldsymbol{P}(\boldsymbol{F})$

$$\overline{\mathbb{A}} = \frac{1}{V} \int_{\mathcal{B}} \mathbb{A}\, dV + \frac{1}{V} \int_{\mathcal{B}} \mathbb{A} : \frac{\partial \widetilde{\boldsymbol{F}}}{\partial \overline{\boldsymbol{F}}}\, dV \,. \tag{89}$$

In the latter equation, the computation of the sensitivity of $\widetilde{\boldsymbol{F}}$ with respect to $\overline{\boldsymbol{F}}$ is the crucial part. Starting from the weak form of the balance of linear momentum at the micro-scale (78) at an equilibrium state, i.e., $G = 0$, then the linearization yields

$$\int_{\mathcal{B}} \delta\widetilde{\boldsymbol{F}} : \mathbb{A} : \Delta\boldsymbol{F}\, dV = 0 \,. \tag{90}$$

Substituting the additive split (87) in (90) yields

$$\underbrace{\int_{\mathcal{B}_0} \delta\widetilde{\boldsymbol{F}} : \mathbb{A} : \Delta\overline{\boldsymbol{F}}\, dV}_{\int_{\mathcal{B}_0} \delta\widetilde{\boldsymbol{F}} : \mathbb{A}\, dV \; : \Delta\overline{\boldsymbol{F}}} + \int_{\mathcal{B}_0} \delta\widetilde{\boldsymbol{F}} : \mathbb{A} : \Delta\widetilde{\boldsymbol{F}}\, dV = 0 \,. \tag{91}$$

The discrete counterpart of the latter equation appears after inserting the approximations of the fluctuation part of the deformation gradient (80) as

$$\sum_{e=1}^{num_{ele}} \delta\widetilde{\boldsymbol{d}}^T \left\{ \underbrace{\int_{\mathcal{B}_0^e} \mathbb{B}^{eT} \mathbb{A}^h \, dV}_{\boldsymbol{l}^e} \, \Delta\overline{\boldsymbol{F}}^h + \underbrace{\int_{\mathcal{B}_0^e} \mathbb{B}^{eT} \mathbb{A}^h \mathbb{B}^e \, dV}_{\boldsymbol{k}^e} \, \Delta\widetilde{\boldsymbol{d}} \right\} = 0 \,, \tag{92}$$

where num_{ele} denotes the number of microscopic finite elements, $\boldsymbol{k}^e$ the element stiffness matrices, see also (83), and $\boldsymbol{l}^e$ the matrices, which take into account the sensitivity of the moduli of the individual finite elements. Thus, in contracted matrix notation, we obtain

$$\sum_{e=1}^{num_{ele}} \left\{ \delta\widetilde{\boldsymbol{d}}^T \left(\boldsymbol{l}^e \, \Delta\overline{\boldsymbol{F}}^h + \boldsymbol{k}^e \Delta\widetilde{\boldsymbol{d}} \right) \right\} = 0 \,. \tag{93}$$

Application of a standard assembling procedure, cf. Eq. (75), yields

$$\delta\widetilde{\boldsymbol{D}}^T \left(\boldsymbol{K} \Delta\widetilde{\boldsymbol{D}} + \boldsymbol{L} \, \Delta\overline{\boldsymbol{F}} \right) = 0 \,. \tag{94}$$

The global stiffness matrix $\boldsymbol{K}$ and the generalized right hand sides $\boldsymbol{L}$ are defined as

$$\boldsymbol{K} = \mathop{\mathsf{A}}_{e=1}^{num_{ele}} \boldsymbol{k}^e \,, \qquad \boldsymbol{L} = \mathop{\mathsf{A}}_{e=1}^{num_{ele}} \boldsymbol{l}^e \,. \tag{95}$$

Formally, the solution of Eq. (94) is achieved by

$$\Delta\widetilde{\boldsymbol{D}} = -\boldsymbol{K}^{-1} \boldsymbol{L} \, \Delta\overline{\boldsymbol{F}}^h \,, \tag{96}$$

which represents the incremental fluctuation field as a consequence of an incremental macroscopic deformation gradient. Inserting the elementwise solutions $\Delta\widetilde{\boldsymbol{d}}$ of (96) in $(80)_3$ and substituting this result into Eq. (89) yields

$$\overline{\mathbb{A}}^h = \underbrace{\frac{1}{V} \sum_{e=1}^{num_{ele}} \int_{\mathcal{B}^e} \mathbb{A}^h \, dV}_{\mathbb{A}^{\text{Voigt}}} + \frac{1}{V} \sum_{e=1}^{num_{ele}} \int_{\mathcal{B}^e} \mathbb{A}^h \, \frac{\partial(\mathbb{B}^e \Delta\widetilde{\boldsymbol{d}})}{\partial\overline{\boldsymbol{F}}^h} \, dV \,, \tag{97}$$

where $\mathbb{A}^{\text{Voigt}}$ denotes the (numerical approximation of the) Voigt upper bound. The second integral term in (97) can be reformulated as

$$\frac{1}{V} \sum_{e=1}^{num_{ele}} \int_{\mathcal{B}^e} \mathbb{A}^h \, \frac{\partial(\mathbb{B}^e \Delta\widetilde{\boldsymbol{d}})}{\partial\overline{\boldsymbol{F}}^h} \, dV = \frac{1}{V} \sum_{e=1}^{num_{ele}} \underbrace{\int_{\mathcal{B}^e} \mathbb{A}^h \mathbb{B}^e \, dV}_{\boldsymbol{l}^{e\star}} \, \frac{\partial\Delta\widetilde{\boldsymbol{d}}}{\partial\overline{\boldsymbol{F}}^h} \,, \tag{98}$$

where $\boldsymbol{l}^{e\star} = \boldsymbol{l}^{eT}$ if $\mathbb{A}$ fullfills the major symmetries, i.e., $\mathbb{A}_{ijkl} = \mathbb{A}_{klij}$. This symmetry relation is provided in the following. After assembling the discrete form, we get with (96) and the linear increment

$$\Delta\overline{\boldsymbol{F}}^h = \overline{\boldsymbol{F}}^h - \overline{\boldsymbol{F}}^h_n \,, \tag{99}$$

based on the nomenclature

$$\overline{\boldsymbol{F}}^h = \overline{\boldsymbol{F}}^h(t_{n+1}) \quad \text{and} \quad \overline{\boldsymbol{F}}^h_n = \overline{\boldsymbol{F}}^h(t_n) \,, \tag{100}$$

the algebraic expression

$$\frac{1}{V}\boldsymbol{L}^T \frac{\partial \Delta\widetilde{\boldsymbol{D}}}{\partial \overline{\boldsymbol{F}}^h} = -\frac{1}{V}\boldsymbol{L}^T\, \boldsymbol{K}^{-1}\boldsymbol{L}\, \frac{\partial \Delta\overline{\boldsymbol{F}}}{\partial \overline{\boldsymbol{F}}^h} = -\frac{1}{V}\boldsymbol{L}^T\, \boldsymbol{K}^{-1}\boldsymbol{L} \,. \tag{101}$$

Thus, the final result for the algorithmic consistent overall moduli is

$$\boxed{\overline{\mathbb{A}} = \mathbb{A}^{\text{Voigt}} - \frac{1}{V}\boldsymbol{L}^T\boldsymbol{K}^{-1}\boldsymbol{L} \quad \text{with} \quad \mathbb{A}^{\text{Voigt}} = \frac{1}{V}\sum_e \int_{\mathcal{B}^e} \mathbb{A}^h \, dV} \,, \tag{102}$$

see Miehe et al. (1999a,b).

In general, huge computational costs in typical direct nonlinear homogenization schemes are governed by using the Newton-Raphson iteration on both scales at each quadrature point. For the efficient computation of the second term in $(102)_1$, we identify

$$\boldsymbol{L}^T\boldsymbol{K}^{-1}\boldsymbol{L} = \boldsymbol{L}^T\mathbb{X}. \tag{103}$$

Here, $\mathbb{X}$ is the solution of a system of equations with several, e.g. nine in 3D, right hand sides which are organized in the matrix $\boldsymbol{L}$:

$$\boldsymbol{K}\mathbb{X} = \boldsymbol{L} \,. \tag{104}$$

For the solution of (103) as well as for the solutions of the weak forms, the sparse structure of all matrices is taken into account.
A study of efficient two-scale homogenization algorithms for nonlinear problems using approximations of the Schur-Complement of the microscopic stiffness matrix based on e.g. LU factorizations is presented in Okada et al. (2010). Several works in the literature are concerned with the derivation of the overall tangent moduli as well as with different approaches (associated to Schur complement computation, perturbation techniques, penalty formulations, Lagrange multiplier methods) useful for efficient computations, in this context we refer to Miehe et al. (1999a), Schröder (2000), Kouznetsova et al. (2001), Miehe and Koch (2002), Miehe (2003), Miehe and Bayreuther (2007), Temizer and Wriggers (2008) and Schröder and Keip (2012).

4 Stability Problems at Different Scales

A challenge in two-scale homogenization techniques is the consideration of instability problems on the different scales, cf. Abeyaratne and Triantafyllidis (1984), Triantafyllidis and Maker (1985), Müller (1987), Geymonat et al. (1993), Miehe et al. (2002), Schröder (2010). In the following, we restrict ourselves to hyperelastic materials and distinguish between structural instabilities and material instabilities. Let

$$\overline{\Pi}(\overline{\boldsymbol{x}}) = \overline{\Pi}^{int}(\overline{\boldsymbol{F}}) + \overline{\Pi}^{ext}(\overline{\boldsymbol{x}}) \tag{105}$$

be the total potential energy of the body of interest on the macro-scale, with

$$\overline{\Pi}^{int}(\overline{\boldsymbol{F}}) = \int_{\overline{\mathcal{B}}_0} \overline{\psi}(\overline{\boldsymbol{F}})\, dV \tag{106}$$

and

$$\overline{\Pi}^{ext}(\overline{\boldsymbol{x}}) = -\int_{\overline{\mathcal{B}}_0} \overline{\boldsymbol{x}} \cdot \overline{\boldsymbol{f}}\, dV - \int_{\partial\overline{\mathcal{B}}_{0,t}} \overline{\boldsymbol{x}} \cdot \overline{\boldsymbol{t}}_0\, dA\ . \tag{107}$$

An equilibrium state, denoted by $\overline{\boldsymbol{x}}^{eq}$, is characterized by an infimum of the total potential energy in the space of admissible functions. The deformation state $\overline{\boldsymbol{x}}^{eq}$ is stable if the inequality

$$\overline{\Pi}(\overline{\boldsymbol{x}}^{ka}) \geq \overline{\Pi}(\overline{\boldsymbol{x}}^{eq}) \quad \forall \text{ kinematically admissible } \overline{\boldsymbol{x}}^{ka} \tag{108}$$

holds and the equality sign only holds for some $\overline{\boldsymbol{x}}^{ka} \neq \overline{\boldsymbol{x}}^{eq}$, see Ogden (1984). The inequality (108) is a sufficient (global) condition for the stability of the equilibrium state $\overline{\boldsymbol{x}}^{eq}$.

For a more suitable criterion, especially from the computational point of view, we restrict our analysis to kinematically admissible functions in the vicinity of $\overline{\boldsymbol{x}}^{eq}$. This means that Eq. (108) becomes an infinitesimal stability criterion, see Truesdell and Noll (1965), chapter 68. The deviation of the total potential energy between an equilibrium state $\overline{\boldsymbol{x}}^{eq}$ and $\overline{\boldsymbol{x}}^{ka}$ is

$$\Delta\overline{\Pi} := \overline{\Pi}(\boldsymbol{x}^{ka}) - \overline{\Pi}(\overline{\boldsymbol{x}}^{eq})\ . \tag{109}$$

For the following remarks, let us recapitulate the first directional derivative of $\overline{\Pi}$ in the direction of $\delta\overline{\boldsymbol{x}}$

$$\frac{d}{d\epsilon}\overline{\Pi}(\overline{\boldsymbol{x}}^{eq} + \epsilon\, \delta\overline{\boldsymbol{x}})\bigg|_{\epsilon=0} =: \overline{G}(\overline{\boldsymbol{x}}^{eq}, \delta\overline{\boldsymbol{x}}^{eq})\ . \tag{110}$$

The second directional derivative of $\overline{\Pi}$, or equivalently the directional derivative of $\overline{G}$, is

$$\frac{d}{d\epsilon}\overline{G}(\overline{\boldsymbol{x}}^{eq}, \delta\overline{\boldsymbol{x}}, \epsilon\, \Delta\overline{\boldsymbol{x}})\bigg|_{\epsilon=0} := \Delta\overline{G}(\overline{\boldsymbol{x}}^{eq}, \delta\overline{\boldsymbol{x}}, \Delta\overline{\boldsymbol{x}})\ . \tag{111}$$

Let us now write $\Delta\overline{\Pi}$, see (109), in terms of a classical Taylor expansion, then we obtain

$$\Delta\overline{\Pi} = \overline{G}(\overline{\boldsymbol{x}}^{eq}, \delta\overline{\boldsymbol{x}}) + \frac{1}{2!}\Delta G(\overline{\boldsymbol{x}}^{eq}, \delta\overline{\boldsymbol{x}}, \Delta\overline{\boldsymbol{x}}) + \frac{1}{3!}\dots \,. \tag{112}$$

In an equilibrium state, $\overline{G}$ is per definition identical to zero, thus, the equilibrium state is stable if

$$\Delta\overline{G}(\overline{\boldsymbol{x}}^{eq}, \delta\overline{\boldsymbol{x}}^{eq}, \Delta\overline{\boldsymbol{x}}) = \int_{\overline{\mathcal{B}}_0} \delta\overline{\boldsymbol{F}} : \overline{\mathbb{A}} : \Delta\overline{\boldsymbol{F}} > 0 \tag{113}$$

holds. More general overviews in this field can be found e.g. in Pflüger (1975) and Thompson and Hunt (1984).

Generalized Convexity Conditions play a major role for the proofs of the existence of minimizing deformations $\boldsymbol{x}$ of the elastic free energy $\psi(\boldsymbol{F})$ of boundary value problems subjected to specific boundary value conditions. A sufficient condition for the existence of minimizers is the sequential-weak lower semicontinuity (s.w.l.s.) and the coercivity of the free energy function. Morrey (1952, 1966) introduced the concept of quasiconvexity, which is formulated as an integral inequality over an arbitrary domain subjected to affine Dirichlet boundary conditions:

[Definition of Quasiconvexity] An elastic stored energy is quasiconvex whenever for all $\mathcal{B} \subset \mathbb{R}^3$, all constant deformation gradients $\overline{\boldsymbol{F}} \in \mathbb{R}^{3\times3}$ and all superposed fluctuation fields $\boldsymbol{w} \in C_0^\infty(\mathcal{B})$ (i.e. with $\boldsymbol{w} = \boldsymbol{0}$ on $\partial\mathcal{B}$) the integral inequality

$$\int_{\mathcal{B}} W(\overline{\boldsymbol{F}} + \mathrm{Grad}\boldsymbol{w})\, dV \geq \int_{\mathcal{B}} W(\overline{\boldsymbol{F}})\, dV = W(\overline{\boldsymbol{F}}) \times \mathrm{Vol}(\mathcal{B}) \tag{114}$$

is valid, Morrey (1952). □

The sequential-lower semicontinuity condition is ensured if the elastic stored energy is quasiconvex and an additional growth condition is fulfilled.

Another very important concept is the polyconvexity introduced by Ball (1977a,b):

[Definition of Polyconvexity] $\boldsymbol{F} \mapsto W(\boldsymbol{F})$ is polyconvex if and only if there exists a function $P : \mathbb{R}^{3\times3} \times \mathbb{R}^{3\times3} \times \mathbb{R} \mapsto \mathbb{R}$ (in general non-unique) such that

$$W(\boldsymbol{F}) = P(\boldsymbol{F}, \mathrm{Cof}\boldsymbol{F}, \det\boldsymbol{F}) \tag{115}$$

and the function $(\boldsymbol{F}, \mathrm{Cof}\boldsymbol{F}, \det\boldsymbol{F}) \in \mathbb{R}^{19} \mapsto P(\boldsymbol{F}, \mathrm{Cof}\boldsymbol{F}, \det\boldsymbol{F}) \in \mathbb{R}$ is convex for all points $\boldsymbol{X} \in \mathbb{R}^3$. □

Polyconvex functions are always s.w.l.s.. Finally, let us recapitulate the notion of Rank-one-convexity and ellipticity:

[Definition of Rank-one convexity] An elastic stored energy is rank-one convex whenever

$$W(\boldsymbol{F} + \lambda \boldsymbol{m} \otimes \boldsymbol{N}_0) \leq \lambda W(\boldsymbol{F} + \boldsymbol{m} \otimes \boldsymbol{N}_0) + (1 - \lambda) W(\boldsymbol{F}) \tag{116}$$

holds for all $\lambda \in [0, 1]$, $\boldsymbol{F} \in \mathbb{R}^{3\times3}$ and all $\boldsymbol{m} \in \mathbb{R}^3, \boldsymbol{N}_0 \in \mathbb{R}^3$ with $\det(\boldsymbol{F} + \lambda \boldsymbol{m} \otimes \boldsymbol{N}_0) > 0$. □

[Definition of Ellipticity] We say that the stored energy $W(\boldsymbol{F}) = \psi(\boldsymbol{C})$ leads to a uniformly elliptical equilibrium system whenever the uniform Legendre-Hadamard condition

$$\exists\, c^+ > 0\,, \forall\, \boldsymbol{F} \in \mathbb{R}^{3\times3}\,, \forall\, \boldsymbol{m}, \boldsymbol{N}_0 \in \mathbb{R}^3 \backslash \{\boldsymbol{0}\} : \\ (\boldsymbol{m} \otimes \boldsymbol{N}_0) : \mathbb{A} : (\boldsymbol{m} \otimes \boldsymbol{N}_0) \geq c^+ \, \|\boldsymbol{m}\|^2 \|\boldsymbol{N}_0\|^2$$

holds. We state that W gives rise to an (strictly) elliptical system if and only if the Legendre-Hadamard condition is valid:

$$\forall\, \boldsymbol{F} \in \mathbb{R}^{3\times3}\,, \forall\, \boldsymbol{m}, \boldsymbol{N}_0 \in \mathbb{R}^3 \backslash \{\boldsymbol{0}\} : \; (\boldsymbol{m} \otimes \boldsymbol{N}_0) : \mathbb{A} : (\boldsymbol{m} \otimes \boldsymbol{N}_0) \geq 0 \; (> 0). \; \square$$

Note that for smooth stored energy functions W strict rank-one convexity implies the strict Legendre-Hadamard condition. A physical interpretation of the aforementioned conditions can be obtained in the context in the field of wave propagation, for more details we refer e.g. to Schröder (2010).

A free energy is materially stable if it is elliptic. A reformulation of the Legendre-Hadamard condition yields

$$(\boldsymbol{m} \otimes \boldsymbol{N}_0) : \mathbb{A} : (\boldsymbol{m} \otimes \boldsymbol{N}_0) = \boldsymbol{m} \cdot \overline{\boldsymbol{Q}}(\boldsymbol{N}_0)\boldsymbol{m} > 0\,, \tag{117}$$

with the accoustic tensor $\overline{\boldsymbol{Q}}$, which is given in index notation by

$$\overline{Q}^{ab} = \mathbb{A}^{aBbD} N_{0B} N_{0D}\,. \tag{118}$$

This means that the accoustic tensor must be positive definite if we want to ensure material stability.

The non-uniqueness of solutions is an inherent feature in finite deformation continuum mechanics. Such problems could occur on both scales, the micro- and the macro-scale. In the following, we focus on microscopic structural instabilities, i.e. on non-stable equilibrium states on the micro-scale, in the context of the micro to macro transition. These phenomena are

associated to convexity properties of the boundary value problems on both scales and their interactions. Following Müller (1987) and Geymonat et al. (1993), we summarize that (i) in case of convex functionals we compute macroscopic energies by

$$\overline{\psi}(\overline{\boldsymbol{F}}) := \inf_{\widetilde{\boldsymbol{w}}} \frac{1}{V_0} \int_{\overline{B}_0} \psi(\overline{\boldsymbol{F}} + \nabla \widetilde{\boldsymbol{w}})\, dV\,, \tag{119}$$

with the fluctuation field $\widetilde{\boldsymbol{w}}$ on *one* unit cell $\mathcal{B}_0$. (ii) Structural instability problems on the micro-scale are associated to the homogenization of a nonconvex boundary value problem on the micro-scale. However, for non-convex functions we have to find in addition the critical size of the representative volume element $\mathcal{B}_0^{crit}$, i.e.

$$\overline{\psi}(\overline{\boldsymbol{F}}) := \inf_{\mathcal{B}_0^{crit}} \left\{ \inf_{\widetilde{\boldsymbol{w}}} \frac{1}{V_0^{crit}} \int_{\mathcal{B}_0^{crit}} \psi(\overline{\boldsymbol{F}} + \nabla \widetilde{\boldsymbol{w}}) dV \right\}\,, \tag{120}$$

with the fluctuation field $\widetilde{\boldsymbol{w}}$ on the representative volume element $\mathcal{B}_0^{crit}$ of critical size. It should be noted that for micro-heterogeneous structures, e.g. for fiber-reinforced matrix materials, the concept of quasiconvexity may not hold. As an illustrative example, we consider the system depicted in Fig. 9 and assume Dirichlet boundary conditions at the outer boundary. Even under affine boundary deformations, as indicated in Fig. 9, we are not able to expect an infimum of the stored energy of the whole system for a constant deformation gradient. On the contrary, we observe a buckling of the fiber for a specific compression state in horizontal direction, which should represent a post-critical stable deformation state.

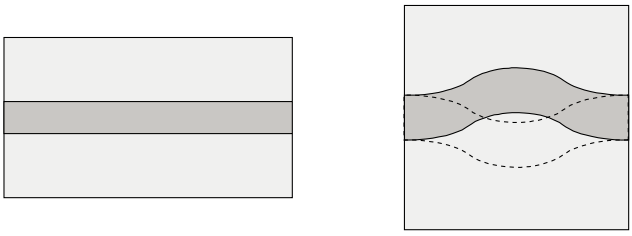

Figure 9. Fiber-reinforced matrix material: Unloaded reference configuration (left) versus buckling of the elastically bedded rod under horizontal compression (right), cf. Marsden and Hughes (1983).

In the following we analyze the influence of the size of the representative volume element (RVE) of a fiber-reinforced microstructure on the macroscopic response at microscopic buckling problems, as discussed in Schröder (2000). A more detailed analysis of instabilities on both scales as well as their interactions are given in Miehe et al. (2002). We consider a homogeneous deformation state at the macro-scale. The considered microstructure consists of a weak matrix (volume faction 80%) with fibers, which are reinforced in horizontal direction, as depicted in Fig. 10a. We expect two classical bifurcation modes, an out-of-phase buckling (Fig. 10b) and an in-phase buckling (Fig. 10c) of the fibers.

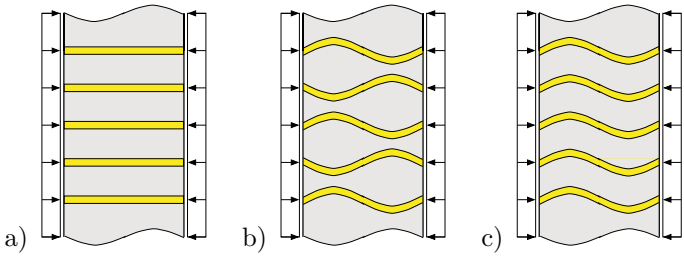

Figure 10. Horizontally loaded fiber reinforced composites: a) reference configuration, b) symmetric (out-of-phase) and c) unsymmetric (in-phase) buckling of the fibers, cf. Schröder (2000).

For simplicity, we apply a standard isotropic St. Venant-Kirchhoff material for the matrix and the fibers and apply periodic boundary conditions. The matrix material has a compression modulus of $\kappa_M = 49.98\, N/mm^2$ and a shear modulus of $\mu_M = 74.97\, N/mm^2$; for the reinforcement we consider the parameters $\kappa_I = 10^4\, \kappa_M$ and $\mu_I = 10^4\, \mu_M$. Applying the macroscopic deformation gradient $\overline{\boldsymbol{F}}$ with

$$\bar{\boldsymbol{F}} = \begin{bmatrix} 1-\lambda & 0 & 0 \\ 0 & 1 & 0 \\ 0 & 0 & 1 \end{bmatrix} \tag{121}$$

represents a horizontal compression state. For the considered compression case, we distinguish, as mentioned above, between two characteristic failure modes: buckling of the reinforcement in-phase (unsymmetric case) and buckling out-of-phase (symmetric case). For the unsymmetric case, we consider a finite-element discretization of an $\mathcal{RVE}$ with one fiber and for the symmetric case a finite-element discretization of an $\mathcal{RVE}$ with two fibers arranged in parallel. The crucial part is the yet unknown size of the $\mathcal{RVE}s$.

Thus, in order to find the critical load value as a function of the length of the discretized microstructure we have to modify the length of the $\mathcal{RVE}s$. For the finite element simulation of the in-phase buckling we discretize the system with 120×20 and for the out-of-phase buckling with 60×40 four-noded standard displacement elements. We start the simulation with a length of $l = 12$ (in consistent units) and increase the length by increments of $\Delta l = 12$ until the value $l = 60$ is reached. Two typical post-critical deformation states for the lengths $l = 6$ and $l = 2$ at the compressions $\lambda = 0.04$ and $\lambda = 0.01$, respectively, are shown in Fig. 11a,b.

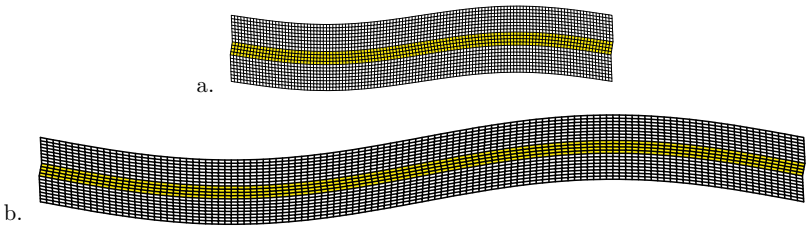

Figure 11. In-phase buckling of the fiber: post-critical deformation state of a) $l = 6$ at a compression parameter $\lambda = 0.04$ and b) $l = 12$ at a compression parameter $\lambda = 0.01$, see Schröder (2000).

The macroscopic Kirchhoff-stresses $\overline{\tau}_{11}$ with respect to the compression parameter λ are depicted in Fig. 12 for different lengths l. With increasing length l, the load-displacement curves are decreasing. Fig. 12b represents the critical stress components $\overline{\tau}_{11,crit}$ at the onset of the microscopic instability. The critical load converges against the lower bound.

For the stability analysis of the out-of-phase buckling mode, we start the simulation with a length $l = 3$ and increase the length stepwise using the increment $\Delta l = 1$ until $l = 12$ is reached.
Fig. 13a shows the macroscopic Kirchhoff-stresses $\overline{\tau}_{11}$ versus the loading paramter λ for eight different lengths. In contrast to the previously discussed in-phase buckling mode, the change of the characteristic curve shape is significant with increasing length. In Fig. 13b, the critical macroscopic stresses $\overline{\tau}_{11,crit}$ are depicted for the onset of the buckling of the fibers. The minimum of the critical stress $\overline{\tau}_{11,crit}$ is obtained at approximately $l = 7$.
Postcritical deformation states for the $\mathcal{RVE}$ of length $l = 5$ at the compression values $\lambda = 0.02$ and $\lambda = 0.03$ are depicted in Fig. 14a,b. A sequence of deformation states for the length $l = 12$ is documented in Fig. 15a–c, for

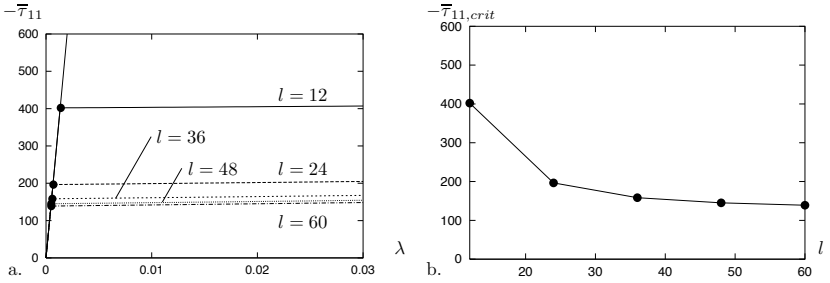

Figure 12. In-phase buckling of the fiber: a) macroscopic Kirchhoff-stresses $\overline{\tau}_{11}$ versus the compression parameter λ and b) critical stress $\overline{\tau}_{11,crit}$ at the onset of the structural instability at the micro-scale versus the length l of the considered microstructure, see Schröder (2000).

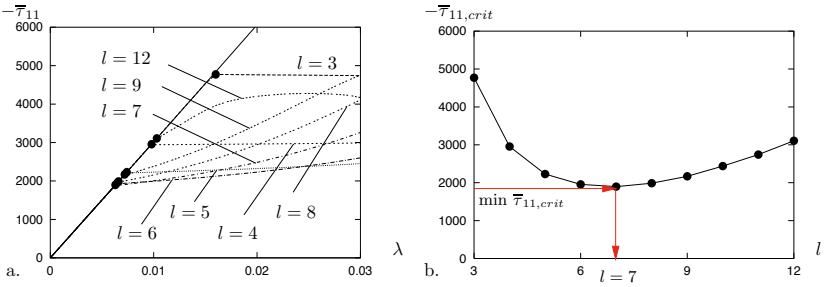

Figure 13. Out-of-phase buckling of the fibers: a) macroscopic Kirchhoff-stresses $\overline{\tau}_{11}$ versus the compression parameter λ for different lengths l and b) critical stress $\overline{\tau}_{11,crit}$ at the onset of the structural instability versus the length l, see Schröder (2000).

the load parameters $\lambda = 0.011, 0.017$ and 0.035, respectively. Additionally, Fig. 15c shows that higher-order buckling modes occur in the case where the length $\mathcal{RVE}$ becomes large enough. Here, three repeating characteristic deformation patterns are observable within the $\mathcal{RVE}$.

The two classical bifurcation modes, in-phase and out-of-phase, show different characteristics in the postcritical regime. In case of the out-of-phase buckling, the fibers support each other at a specific misalignment,

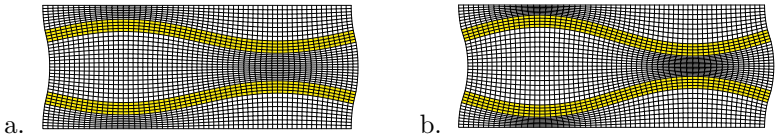

Figure 14. Out-of-phase buckling of the fibers: Post-critical deformation states for $l = 5$ at a compression parameter a) $\lambda = 0.02$ and b) $\lambda = 0.03$, see Schröder (2000).

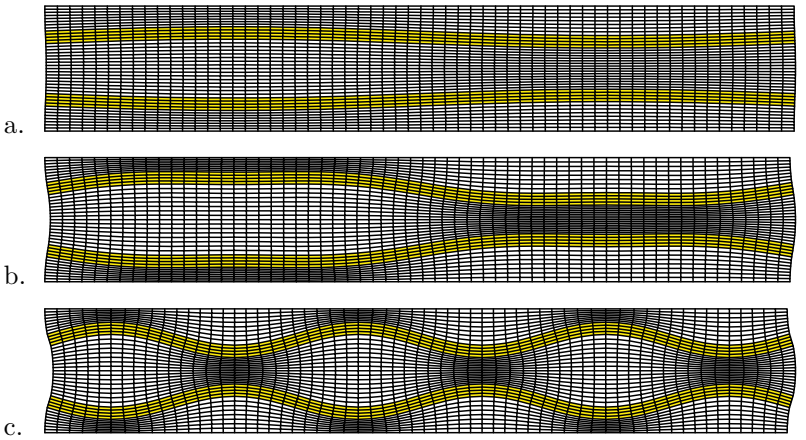

Figure 15. Out-of-phase buckling of the fibers: Post-critical deformation states for length $l = 12$ at a compression parameter a) $\lambda = 0.011$, b) $\lambda = 0.017$ and c) $\lambda = 0.035$, see Schröder (2000).

which leads to an increasing load-deflection curve. Thus, the out-of-phase buckling of the fibers could result in a stabilizing effect, this is in contrast to the postcritical behavior of the in-phase buckling of the fibers.

For a detailed analysis of possible bifurcation modes on the micro-scale as well as associated possible macroscopic material instabilities, we refer to Triantafyllidis and Maker (1985), Müller (1987), Abeyaratne and Triantafyllidis (1984), Triantafyllidis and Maker (1985), Geymonat et al. (1993), Miehe et al. (2002), Aubert et al. (2008), and Agoras et al. (2009) and the references therein.

5 Numerical Studies for Elasto-Plastic $\mathcal{RVE}$s

An important class of micro-heterogeneous materials are modern dual- and multi-phase steels. They exhibit a complex elasto-plastic mechanical response due to the interaction of the different phases in the microstructure. A micrograph of a typical dual-phase steel, a ferrite-perlite steel, is shown in Fig. 16a. The corresponding finite element discretization of this microstructure is depicted in Fig. 16b.

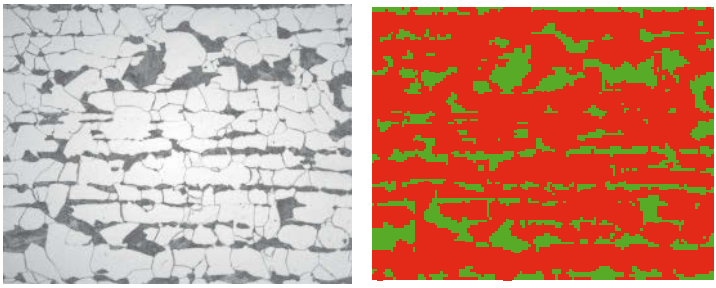

a) b)

Figure 16. Ferrite-Perlite Steel: a) micrograph and b) finite element discretization with 125×100 four noded quadrilateral elements.

In order to demonstrate the complexity of the distribution of the individual fields within the micro-heterogeneous composite, we consider a macroscopic simple tension test under plane strain conditions and apply periodic boundary conditions. For the individual phases, we apply an isotropic J_2-plasictiy model. Fig. 17a,b depict the distributions of the microscopic equivalent

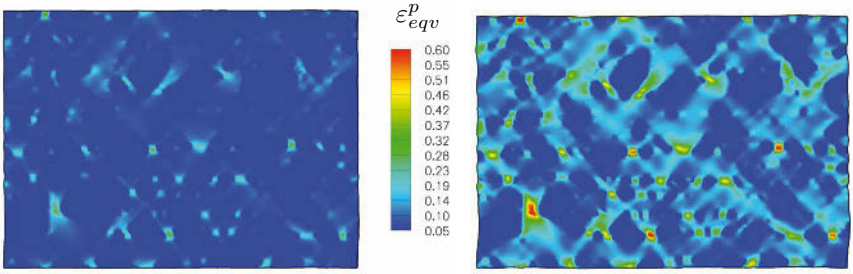

a) b)

Figure 17. Ferrite-Perlite Steel: distribution of equivalent plastic strains under horizontal elongation of a) 5% and b) 10%.

plastic strains for a horizontal elongation of 5% and 10%, respectively.

In this section, we discuss several examples illustrating the influence of different microscopic properties to the macroscopic response, where the numerical analysis is performed with FE^2-simulations.

5.1 Finite J_2-Plasticity Model

The elasto-plastic behavior of the individual constituents at the microscale is described by isotropic finite elasto-plasticity formulations based on the multiplicative decomposition of the deformation gradient

$$\boldsymbol{F} = \boldsymbol{F}^e \, \boldsymbol{F}^p \, , \tag{122}$$

where $\boldsymbol{F}^e$ denotes the elastic and $\boldsymbol{F}^p$ the plastic parts, see Kröner (1960), Lee (1969). For details of the thermodynamical formulation as well as for the numerical treatment, we refer to Simo (1988, 1992), Simo and Miehe (1992), Perić et al. (1992), Miehe and Stein (1992), and Miehe (1993). The strain energy function is assumed to be of the form

$$\psi = \psi^e(\boldsymbol{b}^e) + \psi^p(\alpha) \, , \tag{123}$$

wherein $\boldsymbol{b}^e$ denotes the elastic finger tensor and α the equivalent plastic strains. The elastic finger tensor is defined as

$$\boldsymbol{b}^e = \boldsymbol{F}^e \, (\boldsymbol{F}^e)^T = \sum_{A=1}^{3} (\lambda_A^e)^2 \boldsymbol{n}_A \otimes \boldsymbol{n}_A \tag{124}$$

with the eigenvectors $\boldsymbol{n}_A$ and eigenvalues $(\lambda_A^e)^2$ of the elastic finger tensor $\boldsymbol{b}^e$. Following Simo (1992), we define the strain energy function as

$$\psi^e = \frac{\lambda}{2}[\epsilon_1^e + \epsilon_2^e + \epsilon_3^e]^2 + \mu[(\epsilon_1^e)^2 + (\epsilon_2^e)^2 + (\epsilon_3^e)^2] \tag{125}$$

in terms of the logarithmic elastic strains $\epsilon_A^e = \log(\lambda_A^e)$; λ and μ are the Lamé constants. An exponential-type hardening of the individual phases is modeled by the well-known function

$$\psi^p = y_\infty \alpha - \frac{1}{\eta}(y_0 - y_\infty) \exp(-\eta\alpha) + \frac{1}{2} \, h \, \alpha^2 \, . \tag{126}$$

Herein, y_0 is the initial yield strength, y_∞ and η describe an exponential hardening behavior and h is the slope of a superimposed linear hardening. The yield criterion, formulated in terms of the Kirchhoff stresses

$$\boldsymbol{\tau} = \sum_{A=1}^{3} \tau_A \, \boldsymbol{n}_A \otimes \boldsymbol{n}_A \quad \text{with} \quad \tau_A = \frac{\partial \psi_e}{\partial \epsilon_A^e} \, , \tag{127}$$

is given by the expression

$$\phi = ||\mathrm{dev}\,\boldsymbol{\tau}|| - \sqrt{\frac{2}{3}}\beta \leq 0\,, \tag{128}$$

with

$$\beta = \frac{\partial \psi^p(\alpha)}{\partial \alpha} = y_0 + (y_\infty - y_0)(1 - \exp(-\eta\alpha)) + h\,\alpha\,. \tag{129}$$

The flow rule and the evolution equation for the internal plastic quantity are given by

$$\frac{1}{2}\mathcal{L}(\boldsymbol{b}^e)\boldsymbol{b}^{e\,-1} = -\lambda\frac{\partial\phi}{\partial\boldsymbol{\tau}} \quad \text{and} \quad \dot{\alpha} = \lambda\frac{\partial\phi}{\partial\beta}\,, \tag{130}$$

respectively. Here, $\mathcal{L}$ denotes the Lie time derivative and λ the scalar-valued Lagrange multiplier. The flow rule is integrated using an exponential update algorithm, which preserves plastic incompressibility (Weber and Anand (1990), Simo (1992), and Miehe and Stein (1992)). For the numerical implementation, we follow the algorithmic formulation in a material setting as proposed in Klinkel (2000).

5.2 Shear Test: Comparative Study of Different $\mathcal{RVE}s$.

In the following examples, we consider a (homogeneous) macroscopic pure shear test and analyze the stress-strain relation at the macro-scale for different combinations of constitutive equations of the matrix and the inclusion phase for an artificial $\mathcal{RVE}$. At the macro-scal,e a homogeneous pure shear situation is prescribed by the macroscopic deformation gradient

$$\overline{\boldsymbol{F}} = \begin{bmatrix} 1 & \overline{F}_{12} & 0 \\ \overline{F}_{21} & 1 & 0 \\ 0 & 0 & 1 \end{bmatrix} \quad \text{with} \quad \overline{F}_{12} = \overline{F}_{21}\,. \tag{131}$$

During the simulation, the coefficient $\overline{F}_{12}$ oscillates stepwise between -0.1 and 0.1 in order to simulate a cyclic loading process. It starts with $\overline{F}_{12} = 0.0$ with an increase of the component up to 0.1, this marks the first inflection point. Afterwards the loading is switched and the coefficient is stepwise decreased to -0.1, where the second inflection point is reached. Again, $\overline{F}_{12}$ is increased to 0.1, the next inflection point, and the procedure is repeated. The whole process is controlled by a linear modification of the coefficient $\overline{F}_{12}$ between the coordinates

$$\overline{F}_{12} : 0.0 \rightarrow +0.1 \rightarrow -0.1 \rightarrow +0.1 \rightarrow -0.1 \rightarrow +0.1\,. \tag{132}$$

At the micro-scale, an artificial microstructure is considered, where the inclusion geometry is a *smiley* embedded in a matrix phase. To study

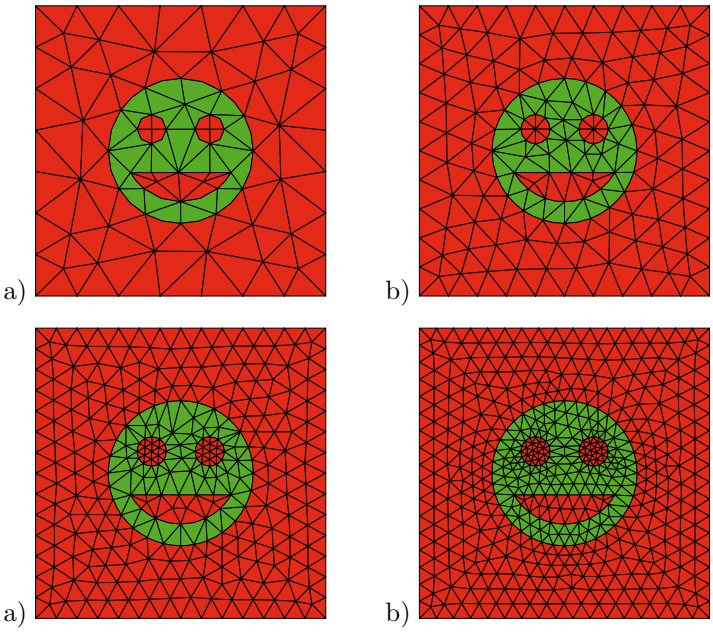

Figure 18. Artificial microstructure with different finite element discretizations: a) 140, b) 292, c) 538 and d) 970 triangular elements with quadratic ansatz functions.

the convergence of the simulation with respect to the element size, four different discretization levels at the micro-scale are used, which consist of 140, 292, 558 and 970 triangular elements with quadratic ansatz functions, cf. Figure 18.

Elastic Matrix and Elastic Inclusion In a first setup, we consider both phases, matrix and inclusion, to be described by a purely elastic material behavior. Thereby, the instantaneous elasticity modulus of the inclusion is assumed to be 1000 times higher than the one of the matrix material; the elasticity parameters for the matrix material are set to

$$\lambda = 118.85 \text{ MPa} \quad \text{and} \quad \mu = 79.230 \text{ MPa} \,. \tag{133}$$

In order to study the influence of the finite element mesh density, we consider the four different discretization levels at the micro-scale depicted in Figure 18.

For the study of the microscopic stress distribution based on the four different discretization levels, the coefficient σ_{12} of the microscopic Cauchy stresses are shown in Figure 19. In the matrix region, no significant differences of the stress distributions are observable. Nevertheless, in the regions close to the inclusion as well as inside the inclusion the stress distributions differ.

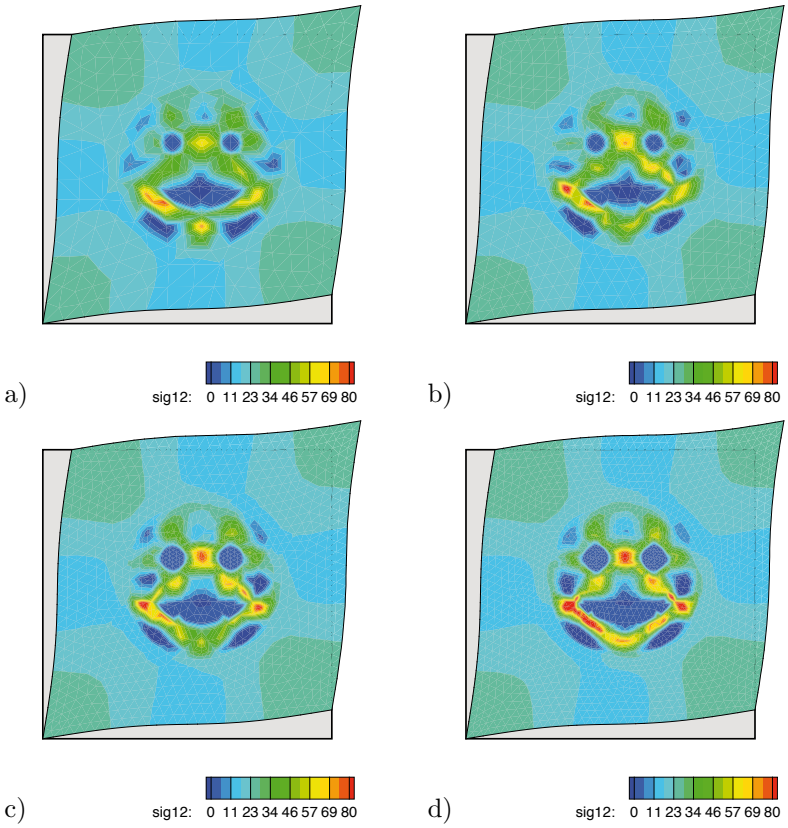

Figure 19. Distribution of the stresses σ_{12} at $\overline{F}_{12} = 0.1$ for different discretizations: a) 140, b) 292, c) 558 and d) 970 elements.

Figure 20a depicts the Cauchy stress σ_{12} versus the shear strain F_{12} for the matrix and the inclusion phase. The macroscopic stress strain curves are practically not influenced by the different mesh densities, see Figure 20b, although at the micro-scale deviations between the simulations can be ob-

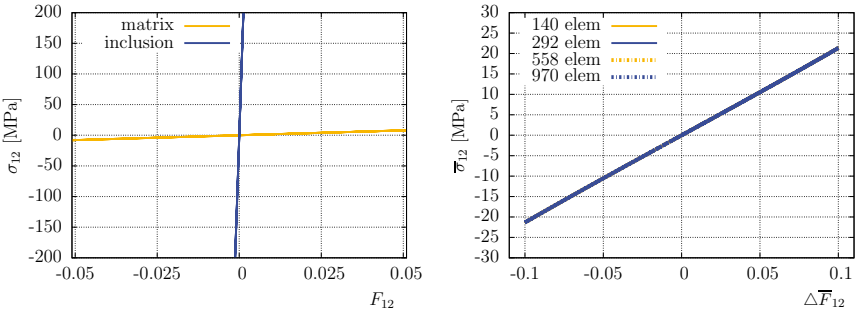

Figure 20. Cauchy stresses versus shear strain: a) σ_{12} versus F_{12} for the individual phases and b) $\overline{\sigma}_{12}$ versus $\overline{F}_{12}$ for the four mesh densities.

served (in this simple example). Therefore, in the following examples we will consider the macroscopic stress-strain relations for all four discretization levels and the local stress distribution at the micro-scale is only depicted for the finest mesh density.

The relative deviation, defined as $e_{\overline{\sigma}_{12}} = (\overline{\sigma}_{12} - \overline{\sigma}_{12}^{[970\ \text{elem}]})/\overline{\sigma}_{12}^{[970\ \text{elem}]}$ for $\overline{\sigma}_{12}^{[970\ \text{elem}]} \neq 0$, of the macroscopic Cauchy stresses with respect to the one obtained using the finest discretization level (970 elements) are depicted in Figure 21. As expected, the deviation of the stresses is decreased along an increasing number of finite elements; nevertheless, the relative error is lower than 0.2%

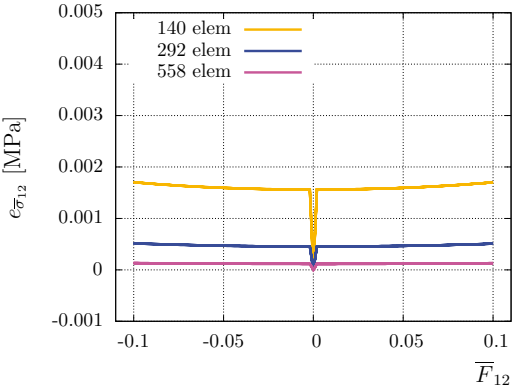

Figure 21. Relative error $e_{\overline{\sigma}_{12}}$ for different discretizations at the micro-scale with respect to the finest discretization level (970 elements).

Elasto-Plastic Matrix and Elastic Inclusion In the following example, we consider again a pure shear test at the macro-scale and also an elastic behavior of the inclusion. With contrast to the previous example, the matrix behavior is now considered to be elasto-plastic. In the elastic domain the same instantaneous elasticity modulus is considered for both phases and for the elasto-plastic behavior of the matrix phase the finite J_2-plasticity model is applied. The material parameters for the matrix material are given in Table 2. The stress-strain relations for the matrix and the inclusion material for the pure shear test are depicted in Figure 22f.

Table 2. Material parameters of the matrix phase.

phase	λ [MPa]	μ [MPa]	y_0 [MPa]	y_∞ [MPa]	η [-]	h [-]
matrix	118,846.2	79,230.77	300.0	300.0	0.0	500.0

The simulations are performed again for the four discretization levels under the pure shear condition described by Eq. (131) and (132). As mentioned in the previous example of pure elastic phases, we represent the distribution of the local fields only for the finest discretization of the $\mathcal{RVE}$ with 970 elements.
Since the matrix phase behaves elasto-plastically, we study the evolution of the equivalent plastic strains α inside this microscopic phase. In Fig. 22a-e, these quantities are shown at the inflection points of the loading. The plastic strains in the matrix phase increase during the whole loading process and in the final state nearly the complete region around the "smiley" exhibits plastic deformation. But inside the "eyes" and the "mouth" the equivalent plastic strains remain at a comparatively low level. This behavior is obvious, since the shape of the inclusion remains nearly undeformed due to its larger stiffness.
In Figure 23a-e, the distribution of the microscopic Cauchy stress coefficient σ_{12} is shown for different loading states, which are obtained by the macroscopic pure shear condition due to the macroscopic deformation tensor given by Equation (131). The macroscopic stress response is nearly the same for all different microscopic discretization levels, cf. Figure 23f. In the inflection points of the loading the microscopic stress components σ_{12} inside most parts of the inclusion phase is larger compared to the matrix phase. Only the region near the "cheeks" of the "smiley" shows lower stress levels.

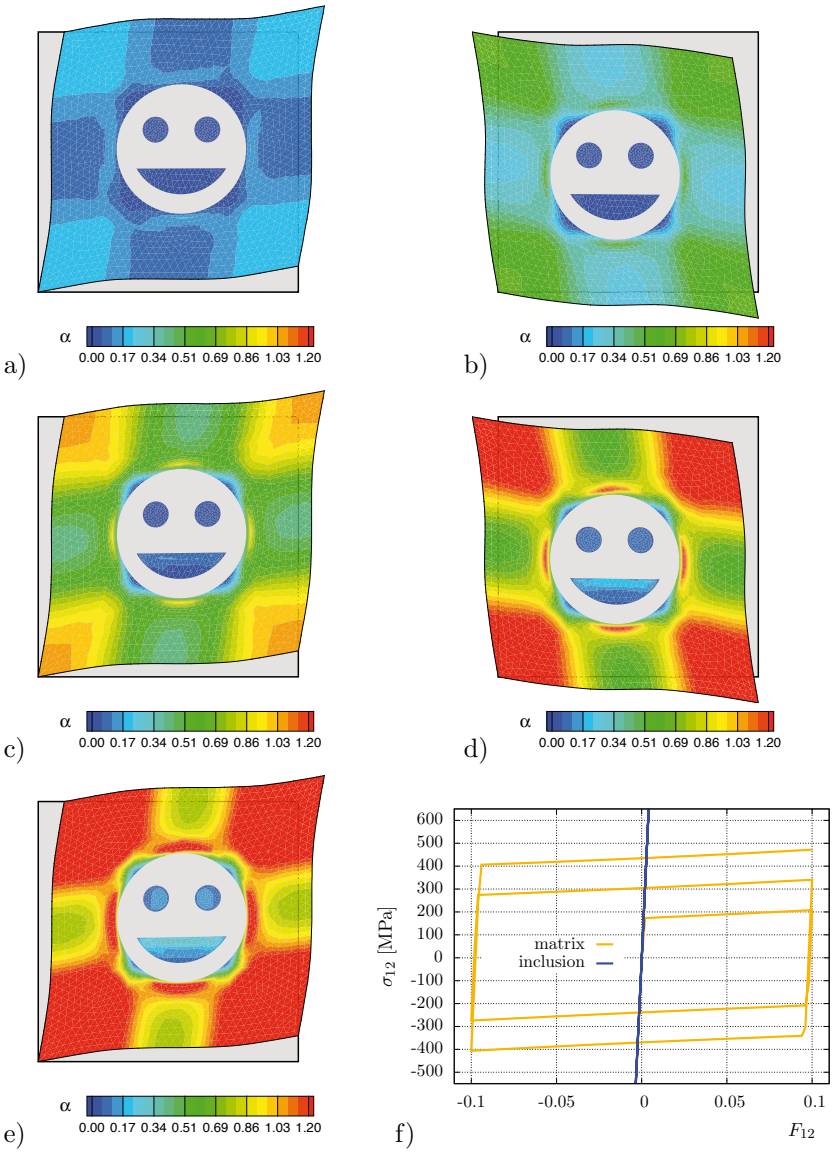

Figure 22. Distribution of the equivalent plastic strains α at the micro-scale (970 elements) with macroscopic deformation gradient coefficient a) $\overline{F}_{12} = 0.1$ in 1^{st} load cycle (l.c.), b) $\overline{F}_{12} = -0.1$ in 1^{st} l.c., c) $\overline{F}_{12} = 0.1$ in 2^{nd} l.c., d) $\overline{F}_{12} = -0.1$ in 2^{nd} l.c., e) $\overline{F}_{12} = 0.1$ in 3^{rd} l.c. The inclusion phase is blanked due to its purely elastic behavior. f) Cauchy stress σ_{12} versus F_{12} for the individual phases.

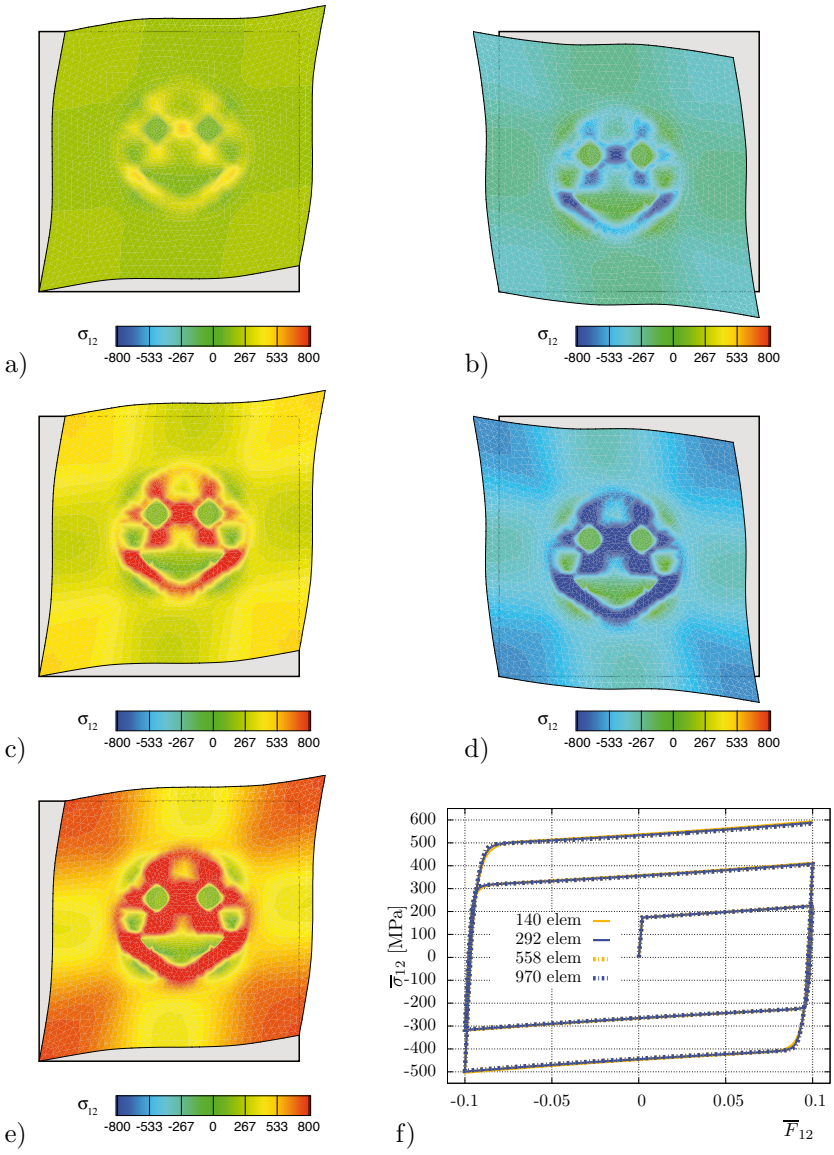

Figure 23. Distribution of the Cauchy stress σ_{12} at the micro-scale (970 elements) with macroscopic deformation gradient coefficient a) $\overline{F}_{12} = 0.1$ in 1st load cycle (l.c.), b) $\overline{F}_{12} = -0.1$ in 1st l.c., c) $\overline{F}_{12} = 0.1$ in 2nd l.c., d) $\overline{F}_{12} = -0.1$ in 2nd l.c., e) $\overline{F}_{12} = 0.1$ in 3rd l.c. and f) macroscopic Cauchy stress $\overline{\sigma}_{12}$ versus $\overline{F}_{12}$ obtained with all microscopic discretization levels.

Elasto-Plastic Matrix and Elasto-Plastic Inclusion Considering the same pure shear situation with a cyclic loading, we study the macroscopic and microscopic mechanical response of the "smiley"-microstructure when both phases, the matrix and the inclusion, behave elasto-plastically. The material model is again described by the set of equations (125)-(127) used with the material parameters given in Table 3. The individual material response of the phases in the pure shear situation is shown in Figure 24f. Note that the parameters are chosen for the inclusion phase such that almost no hardening is obtained during the loading process.

Table 3. Material parameters of the individual phases.

phase	λ [MPa]	μ [MPa]	y_0 [MPa]	y_∞ [MPa]	η [-]	h [-]
matrix	118,846.2	79,230.77	300.0	300.0	0.0	500.0
inclusion	118,846.2	79,230.77	600.0	1000.0	0.0	10.0

Using the four meshes shown in Fig. 18 for the discretization of the "smiley" at the micro-scale, four cyclic loading processes are performed. In Fig. 24a-e, the evolution of the equivalent plastic strains α at the micro-scale is shown in the inflection points and the final state of the loading. At the second and third inflection point the plastic strains are lower almost everywhere in the inclusion phase than in the matrix phase and in the next point this aspect is switched. The reason for this observation becomes obvious if one takes a closer look at the behavior of the individual phases in Fig. 24f. Until the third inflection point, the yield stresses inside the matrix phase are lower than the ones of the inclusion phase, due to the low hardening rate of the inclusion phase. After this point, the relation turns and the plastic strains in the inclusion phase increase. Thus, in the final state the (local averaged) equivalent plastic strains are higher in the inclusion phase than in the matrix phase. The macroscopic mechanical response of the microstructure obtained by the computations using the different discretization levels is depicted in Fig. 25f. The distribution of the microscopic stress components σ_{12} is shown in Fig. 25a-e for all inflection points, where the results of the finest discretization level is used. Again, the different mesh densities provide an almost equal macroscopic response. The microscopic stress distribution correlates inversely to the equivalent plastic strains at the micro-scale. Until the third inflection point, the stress component in the inclusion is higher than in the matrix phase. Afterwards, it turns and the stress distribution in the matrix shows larger values. This effect is also caused by the different hardening properties of the individual phases.

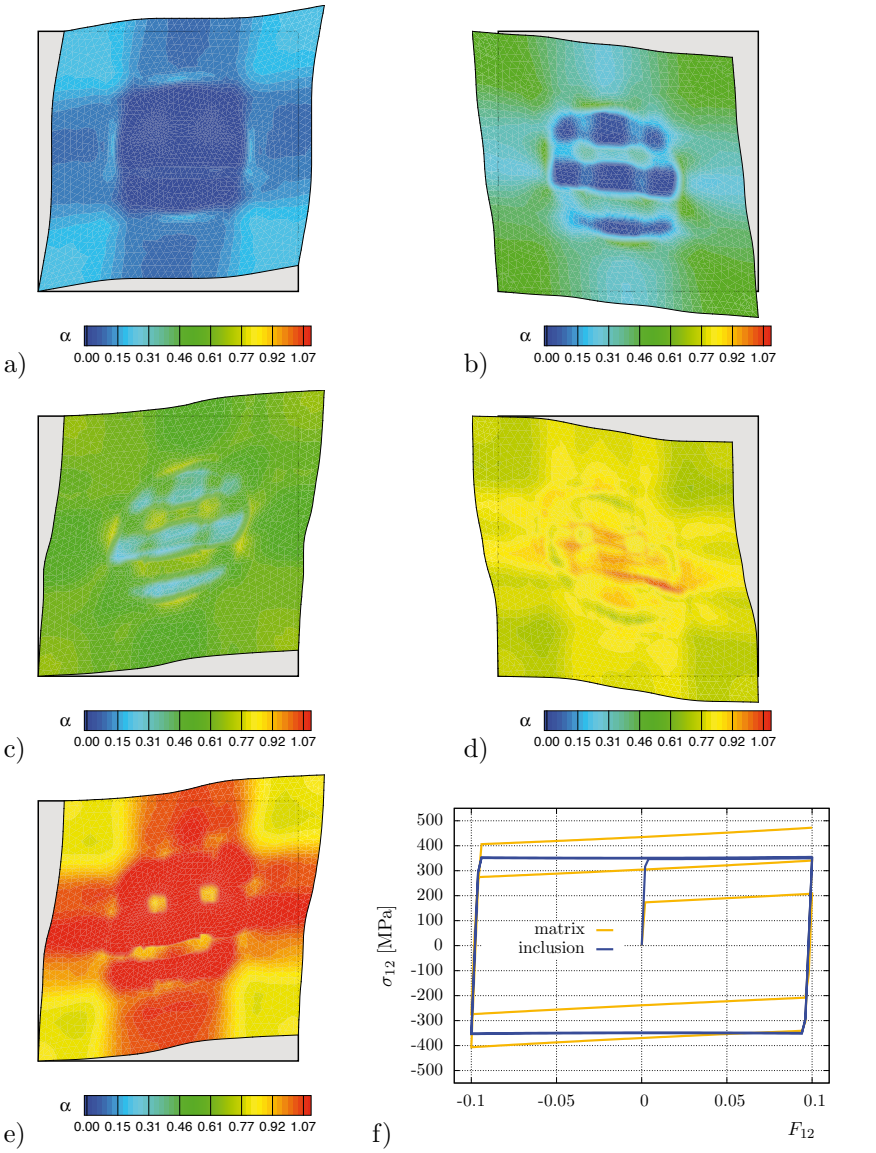

Figure 24. Distribution of the equivalent plastic strains α at the micro-scale (970 elements) with macroscopic deformation gradient coefficient a) $\overline{F}_{12} = 0.1$ in 1st load cycle (l.c.), b) $\overline{F}_{12} = -0.1$ in 1st l.c., c) $\overline{F}_{12} = 0.1$ in 2nd l.c., d) $\overline{F}_{12} = -0.1$ in 2nd l.c., e) $\overline{F}_{12} = 0.1$ in 3rd l.c., and f) Cauchy stress σ_{12} versus F_{12} obtained for the individual phases.

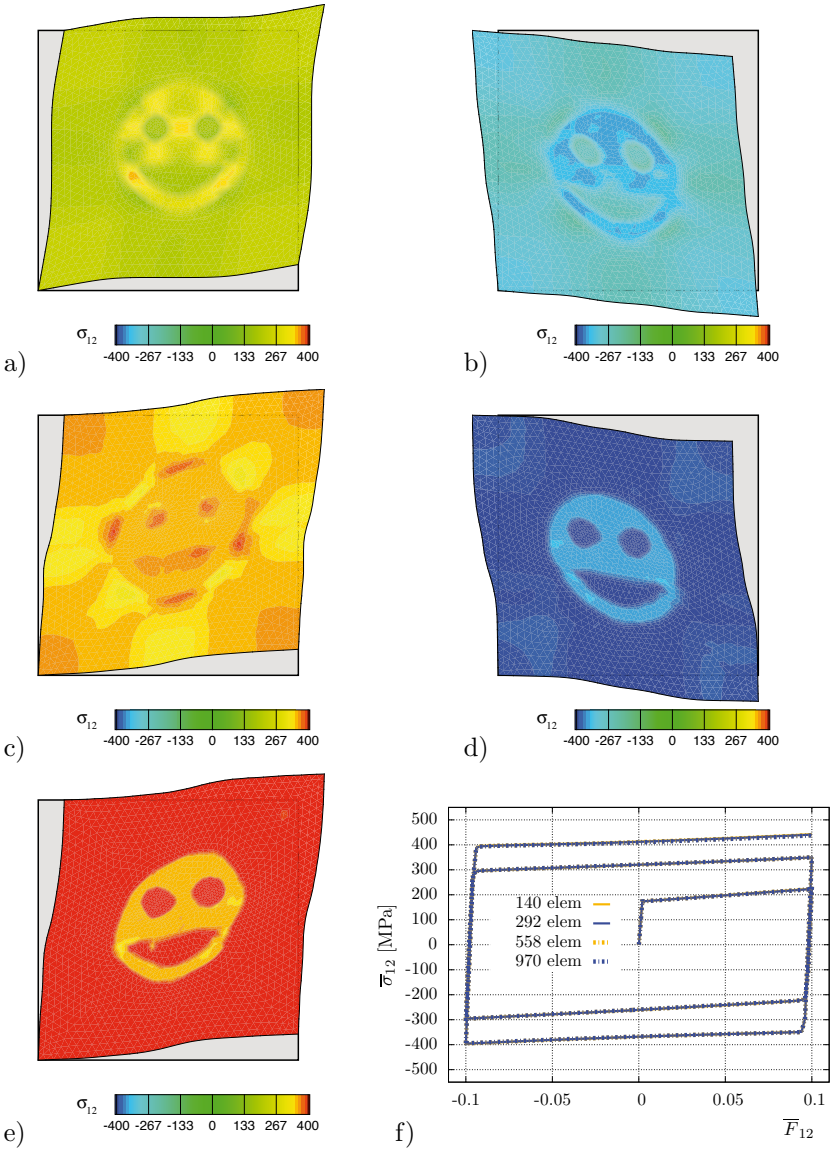

Figure 25. Distribution of the Cauchy stress σ_{12} at the micro-scale (970 elements) with macroscopic deformation gradient coefficient a) $\overline{F}_{12} = 0.1$ in 1^{st} load cycle (l.c.), b) $\overline{F}_{12} = -0.1$ in 1^{st} l.c., c) $\overline{F}_{12} = 0.1$ in 2^{nd} l.c., d) $\overline{F}_{12} = -0.1$ in 2^{nd} l.c., e) $\overline{F}_{12} = 0.1$ in 3^{rd} l.c. and f) macroscopic Cauchy stress $\overline{\sigma}_{12}$ versus $\overline{F}_{12}$ obtained with all microscopic discretization levels.

5.3 Influence of Inclusion Size

The Bauschinger effect, a general phenomenon observed in a variety of polycrystalline metals, describes a yield strength characteristic, denoted as kinematic hardening, as a result of the distribution of the microscopic stress fields. As an example, if the tensile yield strength increases due to tensile loading, the compressive yield strength decreases: we observe a translational movement of the elastic region in stress space. The micromechanical motivation is the assistance of the dislocation movement in reverse loading direction by local back stresses. For the definition of a quantity measuring the Bauschinger, effect several parameters can be found in the literature. Here, a suitable Bauschinger factor is defined as

$$\overline{f}_B = \frac{|\overline{\sigma}^I| - \overline{\sigma}^{II}}{|\overline{\sigma}^I|} \,, \tag{134}$$

for the definition of the individual stress values cf. Fig. 26. This factor is zero for the case where no kinematic hardening occurs and it increases for an increasing kinematic hardening.

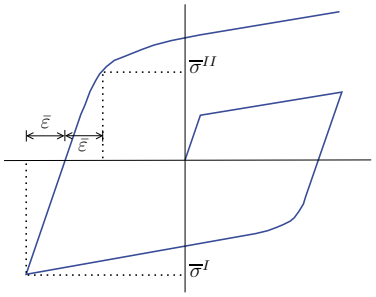

Figure 26. Illustration for the definition of the Bauschinger factor.

In this section, the influence of the inclusion phase fraction on the Bauschinger effect is studied. Thereby, the matrix phase has an elasto-plastic mechanical behavior using the parameters given in Table 4.

Table 4. Material parameters of the matrix phase.

phase	λ [MPa]	μ [MPa]	y_0 [MPa]	y_∞ [MPa]	η [-]	h [-]
matrix	118,846.2	79,230.77	200.0	200.0	0.0	10000.0

The inclusion phase behaves purely elastic with the same instantaneous elasticity modulus as the matrix phase in the elastic domain.

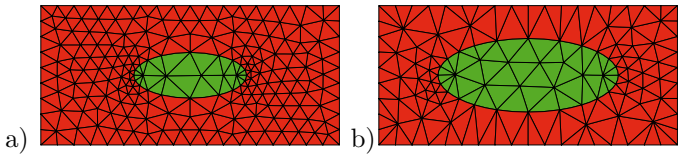

Figure 27. Discretization of the microstructures with a) 10% and b) 25% inclusion phase fraction.

A cyclic tension-compression test is performed at the macro-scale, cf. Fig. 26, and at the micro-scale three different microstructures are considered. The microstructures differ from each other in the phase fraction of the inclusion phase: 0%, 10% and 25%. Consequently, the first configuration is a homogeneous material built from the matrix phase and identical to a purely macroscopic computation using the material parameters of the matrix phase. The inclusion geometry of the second and third one is described by an ellipse. Their discretizations result in two meshes with 386 and 200 triangular finite elements with quadratic shape functions, respectively, cf. Fig. 27a,b.

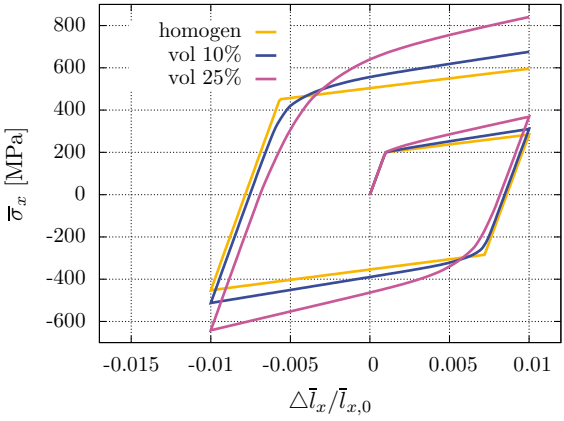

Bauschinger factors:

homogen:
$\overline{f}_B = \frac{450-450}{450} = 0.0$

10% inclusion:
$\overline{f}_B = \frac{510-420}{510} = 0.18$

25% inclusion:
$\overline{f}_B = \frac{640-440}{640} = 0.31$

Figure 28. Macroscopic stress-strain response of the compression-tension test of the homogeneous material and the microstructure with 0%, 10% and 25% inclusion phase fraction and the computed Bauschinger factors, for the definitions cf. Fig. 26.

The macroscopic load scenario involves compression up to $\Delta\overline{l}/\overline{l}_0 = -0.05$, tension back to $\Delta\overline{l}/\overline{l}_0 = 0$ and then further tensile loading. The resulting stress-strain diagrams and the Bauschinger factors computed from that are displayed in Fig. 28. In the homogeneous case, i.e. 0% inclusion phase fraction, the Bauschinger factor is zero, since the material model of the matrix phase does not take into account any kinematic hardening. With an increasing phase fraction of the inclusion phase, the Bauschinger factor also increases to 0.18 and 0.31, respectively, see Fig. 28. Consequently, a significant macroscopic kinematic hardening is observed although no kinematic hardening is considered in the individual phases.

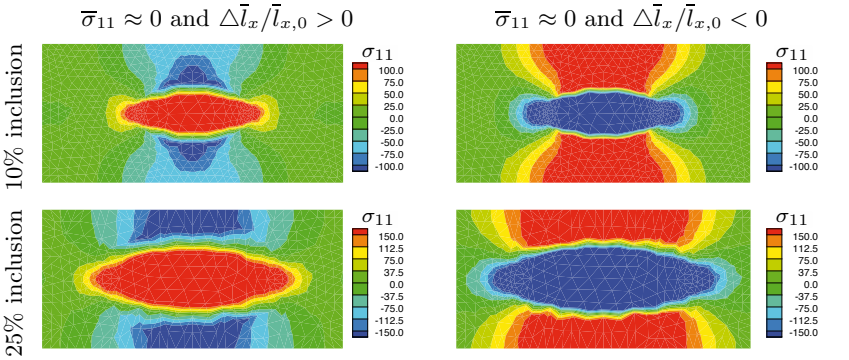

Figure 29. Distribution of the σ_{11}-stress in the macroscopic zero stress states for the microstructures with 10% (bottom row) and 25% (top row) inclusion phase fraction.

To analyze this effect, we take a look at the distribution of the microscopic stress component σ_{11} at the loading point, where the macroscopic stress response is nearly zero, see Fig. 29. These distributions show that in the macroscopic zero stress state the microscopic stresses remain due to the elasto-plastic behavior of the matrix phase. These eigenstresses play a major role for the macroscopic kinematic hardening.

5.4 Notched Rod under Tension

In this section, the mechanical response of a notched rod is analyzed under tensile loading. Thus, we consider now an inhomogeneous boundary value problem on the macro-scale. The geometry of the rod and the boundary conditions are shown in Fig. 30. Associated to the geometric quantities defined therein, we set the length $l = 4.2\,\text{mm}$, the notch radius $r = 0.7\,\text{mm}$, the distance between the notches $d = 1.1\,\text{mm}$ and thus, the height of the rod yields $D = 2.5\,\text{mm}$.

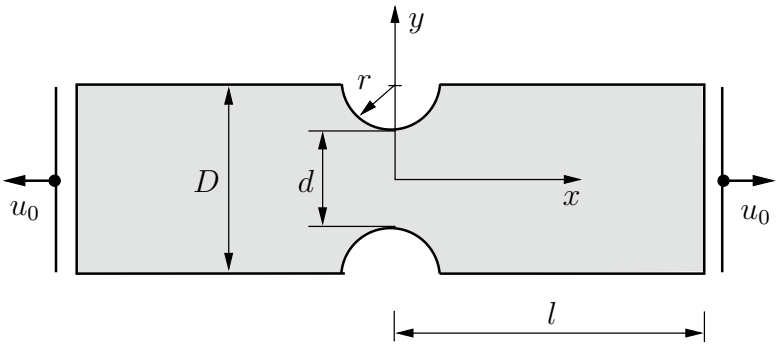

Figure 30. Macroscopic boundary value problem of a notched rod under tensile loading. The vertical degree of freedom of the nodes on the left and right end of the rod are constrained.

Here, a two-dimensional analysis is performed considering plane-strain conditions. The micro-heterogeneity of the underlying material is considered by applying a $\mathcal{RVE}$ at the micro-scale and using the FE^2-method. For this purpose, a real microstructure obtained by image analysis of a micrograph of a Dual-Phase steel as shown in Fig. 31 serves as the $\mathcal{RVE}$. The individual phases (here martensitic island-like inclusions in a ferritic matrix) are modeled by the finite J_2-plasticity model described above incorporating exponential isotropic hardening. The material parameters are chosen such that the matrix and inclusion phase behave similarly to the typical behavior of ferrite and martensite, respectively. As can be seen in Table 5, the elastic Lamé parameters λ and μ are assumed to be the same for both phases and only the plastic parameters are different. At the micro-scale, we consider a discretization with 1548 triangular finite elements, cf. Fig. 31. Linear displacement boundary conditions are taken into account for simplicity. However, a reasonably large $\mathcal{RVE}$ is considered and therefore the impact of the type of boundary conditions should neither significantly influence the macroscopic response, nor the microscopic fields in a reasonable distance from the boundary.

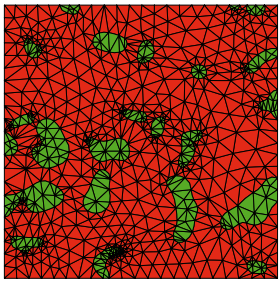

Figure 31. Discretization of the microstructure ($\mathcal{RVE}$) with 1548 quadratic triangular finite elements.

Table 5. Material parameters of the individual phases.

phase	λ [MPa]	μ [MPa]	y_0 [MPa]	y_∞ [MPa]	η [-]	h [-]
matrix	118,846.2	79,230.77	260.0	580.0	9.0	70.0
inclusion	118,846.2	79,230.77	1000.0	2750.0	35.0	10.0

At the macro-scale, the rod is discretized with 528 triangular finite elements, also with quadratic shape functions. The displacements at the macroscopic boundary, as shown in Fig. 30, are increased stepwise until a maximum external displacement of $u_0 = 0.175\,\text{mm}$ is obtained. In total, 2092 load steps are calculated and for each step an average number of 5-7 macroscopic Newton iterations are required. The notched rod in its final deformed configuration is depicted in Fig. 32. In more detail, the von Mises stress distribution is shown indicating the maximum stress values in the center of the rod. At three different macroscopic locations, in the center of the rod, at the boundary of the notch and at the transition of the notch and the rod, local distributions of the equivalent plastic strains are depicted at the microscopic level, see Fig. 32. The locations of those macroscopic integration points are marked by geometric symbols. Whereas the distribution of equivalent plastic strains in the first two microscopic problems are strongly localized with maximum strains of up to 1.2, the third position at the transition between the notch and the straight edge does not exhibit significant plastic strains. Note that a microscopic calculation is run for every macroscopic integration point in a coupled manner and the three microscopic strain distributions shown in Fig. 32 are just three elected situations.

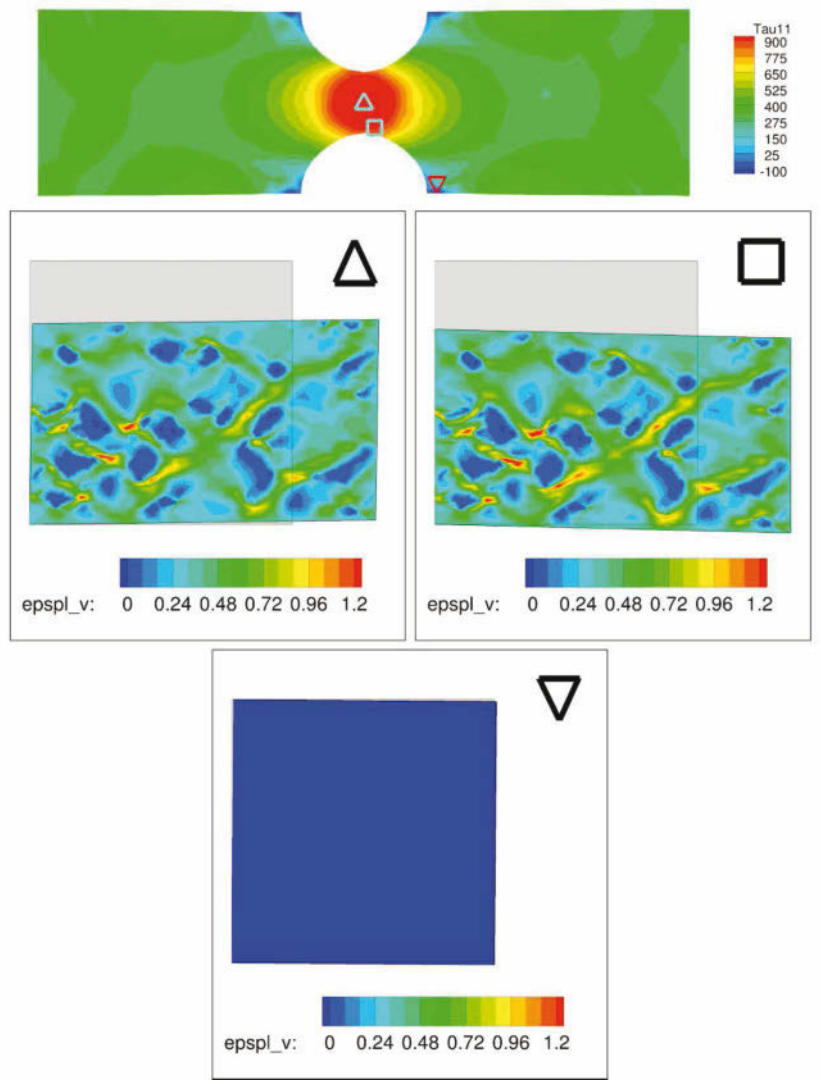

Figure 32. FE^2-simulation: Macroscopic von Mises stress (top), distribution of equivalent plastic strains in the microstructures associated with the three marked macroscopic integration points.

6 Summary and Outlook

In this contribution, we have discussed a direct two-scale homogenization technique, denoted as the FE^2-method or as the multilevel finite element method, for the numerical solution of coupled micro-macro boundary value problems. The presented first-order homogenization scheme seems to be sufficient if the concept of *separation of scales* holds. A fundamental advantage of this scheme is that we do not have to develop (complex) macroscopic constitutive models. Instead of developing such macroscopic phenomenological constitutive laws , we attach representative volume elements ($\mathcal{RVE}$s), reflecting the main characteristics of the underlying microstructure as close as possible, at each point of the macrostructure. In consequence, the macroscopic phenomenological quantities of interest, like stress measures and deformation tensors, are replaced by suitable averages over the microstructure. For this reason we cannot directly compute the macroscopic (overall) algorithmic tangent moduli by the partial derivative of the macroscopic first Piola-Kirchhoff stresses with respect to the macroscopic deformation gradient. In fact, we have to compute this sensitivity in an implicit manner; here we followed the closed-form representation of the macroscopic tangent moduli derived by Miehe et al. (1999a,b).
This general numerical procedure has a wide range of capabilities in the field of classical micro to macro transition problems. In order to demonstrate the performance of this method, we analyzed simple unit cell problems with different stress-strain characteristics for the individual phases of the microstructure. Especially the analysis of complicated processes on the microstructure, taking into account microscopic stress fields, which are responsible for the Bauschinger effect, can be incorporated into the direct homogenization scheme. Furthermore, we have given some remarks concerning structural instabilities on the microstructure and material instabilities on the macrostructure as well as their interactions. In these cases, the size of the attached microstructure plays a crucial role. It was also shown that the procedure solves inhomogeneous macroscopic boundary value problems.

7 Acknowledgements:

Parts of work presented in this contribution are taken from my habilitation thesis and other parts from joint studies with Daniel Balzani and Dominik Brands. The author greatly appreciates the “Deutsche Forschungsgemeinschaft” (DFG) for the financial support under the research grant SCHR 570/8-2 within the research group on “Analysis and Computation of Microstructure in Finite Plasticity”.

Bibliography

R. Abeyaratne and N. Triantafyllidis. An investigation of localization in a porous elastic material using homogenization theory. *Journal of Applied Mechanics*, 51:481–486, 1984.

M. Agoras, O. Lopez-Pamies, and P. Ponte Castañeda. Onset of macroscopic instabilities in fiber-reinforced elastomers at finite strain. *Journal of the Mechanics and Physics of Solids*, 57:1828–1850, 2009.

M. Ambrozinski, K. Bzowski, L. Rauch, and M. Pietrzyk. Application of statistically similar representative volume element in numerical simulations of crash box stamping. *Archives of Cicvil and Mechanical Engineering*, 12:126–132, 2012.

P. Aubert, C. Licht, and S. Pagano. Some numerical simulations of large deformations of heterogeneous hyperelastic materials. *Computational Mechanics*, 41:739–746, 2008.

I. Babuska. Homogenisation approach in engineering. In *Lecture Notes in Economics and Math. Systems*, volume 134, pages 137–153. Springer Verlag, 1976.

N. Bakhvalov and G. Panasenko. *Homogenisation: Averaging processes in periodic media*. Kluwer Academic Publishers, 1984.

J.M. Ball. Convexity conditions and existence theorems in nonlinear elasticity. *Archive for Rational Mechanics and Analysis*, 63:337–403, 1977a.

J.M. Ball. Constitutive inequalities and existence theorems in nonlinear elastostatics. In R. J. Knops, editor, *Symposium on Non-Well Posed Problems and Logarithmic Convexity*, volume 316. Springer-Lecture Notes in Math., 1977b.

D. Balzani, J. Schröder, and D. Brands. FE^2-simulation of microheterogeneous steels based on statistically similar RVEs. In *Proceedings of the IUTAM Symposium on Variational Concepts with applications to the mechanics of materials, September 22-26, 2008, Bochum, Germany*, 2009.

D. Balzani, D. Brands, J. Schröder, and C. Carstensen. Sensitivity analysis of statistical measures for the reconstruction of microstructures based on the minimization of generalized least-square functionals. *Technische Mechanik*, 30:297–315, 2010.

A. Bensoussan, J.L. Lions, and G. Papanicolaou. *Asymptotic Analysis for Periodic Structures*. North-Holland Publishing Company, 1978.

J.D. Clayton and D.L. McDowell. A multiscale multiplicative decomposition for elastoplasticity of polycrystals. *International Journal of Plasticity*, 19:1401–1444, 2003.

E. A. de Souza Neto and R.A. Feijoo. On the equivalence between spatial and material volume averaging of stress in large strain multi-scale solid constitutive models. *Mechanics of Materials*, 40:803–811, 2008.

W.J. Drugan and J.R. Willis. A micromechanics-based nonlocal constitutive equation and estimates of representative volume element size for elastic composites. *Journal of the Mechanics and Physics of Solids*, 44:497–524, 1996.

F. Feyel. A multilevel finite element method (FE^2) to describe the response of highly non-linear structures using generalized continua. *Computer Methods in Applied Mechanics and Engineering*, 192:3233–3244, 2003.

F. Feyel and J.-L. Chaboche. FE^2 multiscale approach for modelling the elastoviscoplastic behavior of long fibre SiC/Ti composite materials. *Computer Methods in Applied Mechanics and Engineering*, 183:309–330, 2000.

J. Fish and A. Wagiman. Multiscale finite element method for a locally nonperiodic heterogeneous medium. *Computational Mechanics*, 12:164–180, 1993.

E. I. Saavedra Flores and E. A. de Souza Neto. Remarks on symmetry conditions in computational homogenisation problems. *International Journal for Computer-Aided Engineering and Software*, 27:551–575, 2010.

S. Forest. Homogenization methods and the mechanics of generalized continua, part 2. *Theoretical and Applied Mechanics*, 28–29:113–143, 2002.

S. Forest and D. K. Trinh. Generalized continua and non-homogeneous boundary conditions in homogenisation methods. *Zeitschrift für angewandte Mathematik und Mechanik*, 91:90–109, 2011.

M.G.D. Geers, V. Kouznetsova, and W.A.M. Brekelmans. Gradient-enhanced computational homogenization for the micro-macro scale transition. *Journal de Physique IV*, 11:145–152, 2001.

M.G.D. Geers, V. Kouznetsova, and W.A.M. Brekelmans. Multi-scale first-order and second-order computational homogenization of microstructures towards continua. *International Journal for Multiscale Computational Engineering*, 1:371–386, 2003.

M.G.D. Geers, E.W.C. Coenen, and V. Kouznetsova. Multi-scale computational homogenization of structured thin sheets. *Modelling and Simulation in Material Science and Engineering*, 15:393–404, 2007.

G. Geymonat, S. Müller, and N. Triantafyllidis. Homogenization of nonlinearly elastic materials, microscopic bifurcation and macroscopic loss of rank-one convexity. *Archive for Rational Mechanics and Analysis*, 122: 231–290, 1993.

S. Ghosh, K. Lee, and S. Moorthy. Multiple scale analysis of heterogeneous elastic structures using homogenization theory and voronoi cell finite element method. *International Journal of Solids and Structures*, 32:27–62, 1995.

F. Gruttmann and W. Wagner. A coupled two-scale shell model with applications to layered structures. *International Journal for Numerical Methods in Engineering*, 2013. accepted for publication.

J.M. Guedes and N. Kikuchi. Preprocessing and postprocessing for materials based on the homogenization method with adaptive finite element methods. *Computer Methods in Applied Mechanics and Engineering*, 83: 143–198, 1990.

Z. Hashin. Analysis of composite materials - a survey. *Journal of Applied Mechanics*, 50:481–505, 1983.

M. Hautefeuille, J.-B. Colliat, A. Ibrahimbegović, H.G. Matthies, and P. Villon. A multi-scale approach to model localized failure with softening. *Computers and Structures*, 94-95:83–95, 2012.

R. Hill. Elastic properties of reinforced solids: some theoretical principles. *Journal of the Mechanics and Physics of Solids*, 11:357–372, 1963.

R. Hill. Theory of mechanical properties of fibre-strengthened materials 1. elastic behaviour. *Journal of the Mechanics and Physics of Solids*, 12: 199–212, 1964a.

R. Hill. Theory of mechanical properties of fibre-strengthened materials 2. inelastic behaviour. *Journal of the Mechanics and Physics of Solids*, 12: 213–218, 1964b.

R. Hill. A self–consistent mechanics of composite materials. *Journal of the Mechanics and Physics of Solids*, 13:213–222, 1965a.

R. Hill. Theory of mechanical properties of fibre-strengthened materials 3. self-consistent model. *Journal of the Mechanics and Physics of Solids*, 13:189–198, 1965b.

R. Hill. On macroscopic measures of plastic work and deformation in microheterogeneous media. *Journal of Applied Mathematics and Mechanics*, 35:31–39, 1971.

R. Hill. On constitutive macro-variables for heterogeneous solids at finite strain. *Proceedings of the Royal Society London A*, 326:131–147, 1972.

R. Hill. On macroscopic effects of heterogeneity in elastoplastic media at finite strain. *Mathematical Proceedings of the Cambridge Philosophical Society*, 95:481–494, 1984.

A. Ibrahimbegović and D. Markovič. Strong coupling methods in multiphase and multi-scale modeling of inelastic behavior of heterogeneous structures. *Computer Methods in Applied Mechanics and Engineering*, 192:3089–3107, 2003.

R. Jänicke, S. Diebels, H. G. Sehlhorst, and A. Düster. Two-scale modeling of micromorphic continua. *Continuum Mechanics and Thermodynamics*, 21:297–315, 2009.

D. Jeulin and M. Ostoja-Starzewski, editors. *Mechanics of random and multiscale microstructures*. Springer, 2001.

T. Kanit, S. Forest, I. Galliet, V. Mounoury, and D. Jeulin. Determination of the size of the representative volume element for random composites: statistical and numerical approach. *International Journal of Solids and Structures*, 40:3647–3679, 2003.

S.O. Klinkel. *Theorie und Numerik eines Volumen-Schalen-Elementes bei finiten elastischen und plastischen Verzerrungen.* PhD thesis, Universität Fridericiana zu Karlsruhe, 2000.

V. Kouznetsova, W.A.M. Brekelmans, and Baaijens F.P.T. An approach to micro-macro modeling of heterogeneous materials. *Computational Mechanics*, 27:37–48, 2001.

V. Kouznetsova, M.G.D. Geers, and W.A.M. Brekelmans. Multi-scale second-order computational homogenization of multi-phase materials: a nested finite element solution strategy. *Computer Methods in Applied Mechanics and Engineering*, 193(48-51):5525–5550, 2004.

E. Kröner. Allgemeine Kontinuumstheorie der Versetzung und Eigenspannung. *Archive of Rational Mechanics and Analysis*, 4:273–334, 1960.

E. Kröner. Statistical continuum mechanics. In *CISM Courses and Lectures*, volume 92. Springer-Verlag, Wien, New-York, 1971.

F. Larsson, K. Runesson, S. Saroukhani, and R. Vafadari. Computational homogenization based on a weak format of micro-periodicity for RVE-problems. *Computer Methods in Applied Mechanics and Engineering*, 200:11–26, 2011.

E.H. Lee. Elasto-plastic deformation at finite strains. *Journal of Applied Mechanics*, 36:1–6, 1969.

J. Mandel. *Plasticité cassique et Viscoplasticité.* Number 97 in CISM lecture notes. Springer, 1972.

J. Mandel and P. Dantu. Contribution à l'étude théorique et expérimentale du coefficient d'élasticité d'un milieu hétérogène mais statistiquement homogène. *Anales des Ponts et Chaussées Paris*, 133(2):115–146, 1963.

D. Markovic, R. Niekamp, A. Ibrahimbegovic, H.G. Matthies, and R.L. Taylor. Multi-scale modeling of heterogeneous structures with inelastic constitutive behaviour: Part I - physical and mathematical aspects. *Engineering Computations*, 22(5-6):664–683, 2005.

J.E. Marsden and J.R. Hughes. *Mathematical Foundations of Elasticity.* Prentice-Hall, 1983.

J.C. Michel, H. Moulinec, and P. Suquet. Effective properties of composite materials with periodic microstructure: a computational approach. *Computer Methods in Applied Mechanics and Engineering*, 172:109–143, 1999.

C. Miehe. *Kanonische Modelle multiplikativer Elasto-Plastizität. Thermodynamische Formulierung und Numerische Implementation.* 1993. Habilitationsschrift.

C. Miehe. Computational micro-to-macro transitions for discretized microstructures of heterogeneous materials at finite strains based on the minimization of averaged incremental energy. *Computer Methods in Applied Mechanics and Engineering*, 192:559–591, 2003.

C. Miehe and C.G. Bayreuther. On mutiscale FE analyses of heterogeneous structures: from homogenization to multigrid solvers. *International Journal for Numerical Methods in Engineering*, 71:1135–1180, 2007.

C. Miehe and A. Koch. Computational micro-to-macro transitions of discretized microstructures undergoing small strains. *Archive of Applied Mechanics*, 72(4):300–317, 2002.

C. Miehe and E. Stein. A canonical model of multiplicative elasto-plasticity formulation and aspects of the numerical implementation. *European Journal of Mechanics, A/Solids*, 11:25–43, 1992.

C. Miehe, J. Schotte, and J. Schröder. Computational micro-macro transitions and overall moduli in the analysis of polycrystals at large strains. *Computational Materials Science*, 16(1-4):372–382, 1999a.

C. Miehe, J. Schröder, and J. Schotte. Computational homogenization analysis in finite plasticity. Simulation of texture development in polycrystalline materials. *Computer Methods in Applied Mechanics and Engineering*, 171(3-4):387–418, 1999b.

C. Miehe, J. Schröder, and M. Becker. Computational homogenization analysis in finite elasticity: Material and structural instabilities on the micro- and macro-scales of periodic composites and their interaction. *Computer Methods in Applied Mechanics and Engineering*, 191:4971–5005, 2002.

C.B. Morrey. Quasi-convexity and the lower semicontinuity of multiple integrals. *Pacific Journal of Mathematics*, 2:25–53, 1952.

C.B. Morrey. *Multiple integrals in the calculus of variations.* Springer, 1966.

S. Müller. Homogenization of nonconvex integral functionals and cellular elastic materials. *Archive for Rational Mechanics and Analysis*, 99:189–212, 1987.

S. Müller and S. Neukamm. On the commutability of homogenization and linearization in finite elasticity. *Archive for Rational Mechanics and Analysis*, 201:465–500, 2011.

S. Nemat-Nasser. Averaging theorems in finite deformation plasticity. *Mechanics of Materials*, 31:493–523, 1999.

S. Nemat-Nasser and M. Hori. *Micromechanics: Overall Properties of Heterogeneous Materials.* North Holland, 2 edition, 1999.

R. Niekamp, D. Markovic, A. Ibrahimbegovic, H.G. Matthies, and R.L. Taylor. Multi-scale modelling of heterogeneous structures with inelastic constitutive behavior: Part II - software coupling implementation aspects. *Engineering Computations*, 26(1/2):6–28, 2009.

R.W. Ogden. *Non-linear elastic deformations.* Dover Publications, 1984.

N. Ohno, T. Matsuda, and X. Wu. A homogenization theory for elastic-viscoplastic composites with point symmetry of internal distributions. *International Journal of Solids and Structures*, 38:2867–2878, 2001.

N. Ohno, D. Okumura, and H. Noguchi. Microscopic symmetric bifurcation condition of cellular solids based on a homogenization theory of finite deformation. *Journal of the Mechanics and Physics of Solids*, 50:1125–1153, 2002.

J. Ohser and F. Mücklich. *Statistical analysis of microstructures in materials science*. J Wiley & Sons, 2000.

J. Okada, T. Washio, and T. Hisada. Study of efficient homogenization algorithms for nonlinear problems – approximation of a homogenized tangent stiffness to reduce computational cost. *Computational Mechanics*, 46:247–258, 2010.

M. Ostoja-Starzewski. Material spatial randomness: From statistical to representative volume element. *Probabilistic Engineering Mechanics*, 21: 112–132, 2006.

M. Ostoja-Starzewski. The use, misuse, and abuse of stochastic random media. In *Proceedings of European Conference on Computational Mechanics*, 2001.

M. Ostoja-Starzweski. *Microstructural randomness and scaling in mechanics of materials*. CRC Series: Modern mechanics and mathematics. Chapman & Hall, 2008.

I. Özdemir, W.A.M. Brekelmans, and M.G.D. Geers. Computational homogenization for heat conduction in heterogeneous solids. *International Journal for Numerical Methods in Engineering*, 73:185–204, 2008.

D. Perić, D.R.J. Owen, and M.E. Honnor. A model for finite strain elasto-plasticity based on logarithmic strains: Computational issues. *Computer Methods in Applied Mechanics and Engineering*, 94:35–61, 1992.

D. Perić, E.A. de Souza Neto, R.A. Feijóo, M. Partovi, and A.J. Carneiro Molina. On micro-to-macro transitions for multi-scale analysis of non-linear heterogeneous materials: unified variational basis and finite element implementation. *International Journal for Numerical Methods in Engineering*, 87:149–170, 2011.

A. Pflüger. *Stabilitätsprobleme in der Elastostatik*. Springer-Verlag, 1975.

G.L. Povirk. Incorporation of microstructural information into models of two-phase materials. 43/8:3199–3206, 1995.

A. Reuss. Berechnung der Fließgrenze von Mischkristallen auf Grund der Plastizitätsbedingung für Einkristalle. *Zeitschrift für angewandte Mathematik und Mechanik*, 9(1):49–58, 1929.

I. Saiki, K. Terada, K. Ikeda, and M. Hori. Appropriate number of unit cells in a representative volume element for micro-structural bifurcation encountered in a multi-scale modeling. *Computer Methods in Applied Mechanics and Engineering*, 191:2561–2585, 2002.

E. Sanchez-Palencia and A. Zaoui. *Lecture notes in physics: Homogenization techniques for composite media*. Springer–Verlag, Berlin, 1986.

J. Schröder. *Homogenisierungsmethoden der nichtlinearen Kontinuumsmechanik unter Beachtung von Stabilitätsproblemen*. Bericht aus der Forschungsreihe des Instituts für Mechanik (Bauwesen), Lehrstuhl I, Universität Stuttgart, 2000. Habilitation.

J. Schröder. Derivation of the localization and homogenization conditions for electro-mechanically coupled problems. *Computational Materials Science*, 46(3):595–599, 2009.

J. Schröder. Anisotropic polyconvex energies. In J. Schröder and P. Neff, editors, *Poly-, Quasi- and Rank-One Convexity in Applied Mechanics*, number 516 in CISM Courses and Lectures, pages 53–105. Springer-Verlag, 2010.

J. Schröder and M.-A. Keip. Multiscale modeling of electro-mechanically coupled materials: homogenization procedure and computation of overall moduli. In M. Kuna and A. Ricoeur, editors, *IUTAM Symposium on Multiscale Modelling of Fatigue, Damage and Fracture in Smart Materials*, volume 24 of *IUTAM Bookseries*, pages 265–276. Springer, Netherlands, 2011. ISBN 978-90-481-9887-0.

J. Schröder and M.-A. Keip. Two-scale homogenization of electromechanically coupled boundary value problems – consistent linearization and applications. *Computational Mechanics*, 50(2):229–244, 2012.

J. Schröder, D. Balzani, and D. Brands. Approximation of random microstructures by periodic statistically similar representative volume elements based on lineal-path functions. *Archive of Applied Mechanics*, 81 (7):975–997, 2010.

J.C. Simo. A framework for finite strain elastoplasticity based on maximum plastic dissipation and the multiplicative decomposition: Part I. continuum formulation. *Computer Methods in Applied Mechanics and Engineering*, 66:199–219, 1988.

J.C. Simo. Algorithms for static and dynamic multiplicative plasticity that preserve the classical return mapping schemes of the infinitesimal theory. *Computer Methods in Applied Mechanics and Engineering*, 99:61–112, 1992.

J.C. Simo and C. Miehe. Associative coupled thermoplasticity at finite strains: formulation, numerical analysis and implementation. *Computer Methods in Applied Mechanics and Engineering*, 96:133–171, 1992.

R.J.M. Smit, W.A.M. Brekelmans, and H.E.H. Meijer. Prediction of the mechanical behavior of nonlinear heterogeneous systems by multi-level finite element modeling. *Computer Methods in Applied Mechanics and Engineering*, 155:181–192, 1998.

M. Stroeven and L.J. Askes, H. Sluys. Numerical determination of representative volumes for granular materials. *Computer Methods in Applied Mechanics and Engineering*, 193:3221–3238, 2004.

M. Stroeven, H. Askes, and L.J. Sluys. A numerical approach to determine representative volumes for granular materials. In *Fifth World Congress on Computational Mechanics (WCCM V)*. Vienna University of Technology, 2002.

P.M. Suquet. Elements of homogenization for inelastic solid mechanics. In *Homogenization techniques for composite materials*, Lecture notes in physics 272, chapter 4, pages 193–278. Springer–Verlag, 1987.

S. Swaminathan, S. Ghosh, and N.J. Pagano. Statistically equivalent representative volume elements for unidirectional composite microstructures: part i - without damage. *Journal of Composite Materials*, 40:583–604, 2006.

L. Tartar. *The general theory of homogenization*. Lecture notes of the unione mathematica italiana. Springer–Verlag, 2000.

I. Temizer. On the asymptotic expansion treatment of two-scale finite thermoelasticity. *International Journal of Engineering Science*, 53:74–84, 2012.

I. Temizer and P. Wriggers. On the computation of the macroscopic tangent for multiscale volumetric homogenization problems. *Computer Methods in Applied Mechanics and Engineering*, 198:495–510, 2008.

I. Temizer and T.I. Zohdi. A numerical method for homogenization in nonlinear elasticity. *Computational Mechanics*, 40:281–298, 2007.

K. Terada and N. Kikuchi. A class of general algorithms for multi-scale analyses of heterogeneous media. *Computer Methods in Applied Mechanics and Engineering*, 190(40-41):5427–5464, 2001.

K. Terada, M. Hori, T. Kyoya, and N. Kikuchi. Simulation of the multi-scale convergence in computational homogenization approach. *International Journal of Solids and Structures*, 37:2285–2311, 2000.

K. Terada, I. Saiki, K. Matsui, and Y. Yamakawa. Two-scale kinematics and linearization for simultaneous two-scale analysis of periodic heterogeneous solids at finite strain. *Computer Methods in Applied Mechanics and Engineering*, 192(31-32):3531–3563, 2003.

J.M.T. Thompson and G.W. Hunt. *Elastic Instability Phenomena*. John Wiley & Sons Ltd., 1984.

N. Triantafyllidis and B.N. Maker. On the comparison between microscopic and macroscopic instability mechanisms in a class of fiber-reinforced composites. *Journal of Applied Mechanics*, 52:794–800, 1985.

C. Truesdell and W. Noll. The nonlinear field theories of mechanics. In S. Flügge, editor, *Encyclopedia of Physics*, volume III/3. Springer, 1965.

O. van der Sluis, P.J.G. Schreurs, W.A.M. Brekelmans, and H.E.H. Meijer. Overall behavior of heterogeneous elastoviscoplastic materials: effect of microstructural modelling. *Mechanics of Materials*, 32:449–462, 2000.

W. Voigt. *Lehrbuch der Kristallphysik*. Teubner, 1910.

G. Weber and L. Anand. Finite deformation constitutive equations and a time integration procedure for isotropic, hyperelastic-viscoelastic solids. *Computer Methods in Applied Mechanics and Engineering*, 79:173–202, 1990.

Z. Xia, Y. Zhang, and F. Ellyin. A unified periodical boundary conditions for representative volume elements of composites and applications. *International Journal of Solids and Structures*, 40:1907–1921, 2003.

J. Zeman. *Analysis of Composite Materials with Random Microstructure*. PhD thesis, University of Prague, 2003.

T.I. Zohdi and P. Wriggers. *Introduction to Computational Micromechanics*, volume 20 of *Lecture Notes in Applied and Computational Mechanics*. Springer, 2005.